SANDIA REPORT
SAND2010-6784
Unlimited Release
Printed September 2010

Solid Oxide Electrochemical Reactor Science

Connor J. Moyer, Andrea Ambrosini, Neal P. Sullivan, Robert J. Kee, Ellen B. Stechel

Prepared by
Sandia National Laboratories
Albuquerque, New Mexico 87185 and Livermore, California 94550

Sandia National Laboratories is a multi-program laboratory managed and operated by Sandia Corporation, a wholly owned subsidiary of Lockheed Martin Corporation, for the U.S. Department of Energy's National Nuclear Security Administration under contract DE-AC04-94AL85000.

Approved for public release; further dissemination unlimited.

Sandia National Laboratories

Issued by Sandia National Laboratories, operated for the United States Department of Energy by Sandia Corporation.

NOTICE: This report was prepared as an account of work sponsored by an agency of the United States Government. Neither the United States Government, nor any agency thereof, nor any of their employees, nor any of their contractors, subcontractors, or their employees, make any warranty, express or implied, or assume any legal liability or responsibility for the accuracy, completeness, or usefulness of any information, apparatus, product, or process disclosed, or represent that its use would not infringe privately owned rights. Reference herein to any specific commercial product, process, or service by trade name, trademark, manufacturer, or otherwise, does not necessarily constitute or imply its endorsement, recommendation, or favoring by the United States Government, any agency thereof, or any of their contractors or subcontractors. The views and opinions expressed herein do not necessarily state or reflect those of the United States Government, any agency thereof, or any of their contractors.

Printed in the United States of America. This report has been reproduced directly from the best available copy.

Available to DOE and DOE contractors from
U.S. Department of Energy
Office of Scientific and Technical Information
P.O. Box 62
Oak Ridge, TN 37831

Telephone: (865) 576-8401
Facsimile: (865) 576-5728
E-Mail: reports@adonis.osti.gov
Online ordering: http://www.osti.gov/bridge

Available to the public from
U.S. Department of Commerce
National Technical Information Service
5285 Port Royal Rd.
Springfield, VA 22161

Telephone: (800) 553-6847
Facsimile: (703) 605-6900
E-Mail: orders@ntis.fedworld.gov
Online order: http://www.ntis.gov/help/ordermethods.asp?loc=7-4-0#online

SAND2010-6784
Unlimited Release
Printed September 2010

Solid Oxide Electrochemical Reactor Science

Andrea Ambrosini, Ellen B. Stechel
Org. 6364: Materials, Devices & Energy Tech
Sandia National Laboratories
P.O. Box 5800
Albuquerque, New Mexico 87185-MS0734

Connor J. Moyer, Neal P. Sullivan, Robert J. Key
Colorado School of Mines
Golden, Colorado, USA 80401

Abstract

This LDRD involved a collaboration between Sandia and the Colorado School of Mines (CSM) ins solid-oxide electrochemical reactors targeted at solid oxide electrolyzer cells (SOEC), which are the reverse of solid-oxide fuel cells (SOFC). SOECs complement Sandia's efforts in thermo-chemical production of alternative fuels. An SOEC technology would co-electrolyze carbon dioxide (CO_2) with steam at temperatures around 800 ºC to form synthesis gas (H_2 and CO), which forms the building blocks for a petrochemical substitutes that can be used to power vehicles or in distributed energy platforms. The effort described here concentrates on research concerning catalytic chemistry, charge-transfer chemistry, and optimal cell-architecture. technical scope included computational modeling, materials development, and experimental evaluation. The project engaged the Colorado Fuel Cell Center at CSM through the support of a graduate student (Connor Moyer) at CSM and his advisors (Profs. Robert Kee and Neal Sullivan) in collaboration with Sandia.

ACKNOWLEDGMENTS

This report is based largely upon the thesis written by Connor Moyer for his degree of Master of Science (Engineering) at Colorado School of Mines, which this LDRD helped fund. This project also leveraged modeling results from Dr. Huayang Zhu at Colorado School of Mines, who was primarily funded by the Office of Naval Research via an RTC grant (N00014-05-1-03339).

CONTENTS

1. Introduction 9
1.1. Background 9
1.2 Motivation 11
1.3 Approach 12
2. Background 13
2.1 Hydrogen/Syngas Production Options 13
2.2 Materials Development 13
2.2.1. Electrolyte Materials 14
2.2.1 Fuel Electrode 15
2.2.3 Air Electrode 15
2.3 Electrolysis Degradation 16
2.4 Charge-Transfer Chemistry 17
2.4.1 Mizusaki Patterned Electrode Experiments 17
2.4.2 Sukeshini CO/H_2 Oxidation on Patterned Electrodes 18
2.4.3 Goodwin Electrochemical Oxidation Modeling 20
3. Experimental Method 21
3.1 Planar Cell Fabrication 21
3.2 Tubular Cell Fabrication 23
3.3 Electrochemical Performance Measurements 23
3.4 Gas Flow Rates and Utilization 26
4. Computational Model 29
4.1 Overview 29
4.2 Reaction and Charge-Transfer Mechanisms 30
5. Results and Analysis 35
5.1 H_2-H_2O Mixture Polarization Behavior 36
5.2 Effect of CO/CO_2 Addition 37
5.3 Effect of Charge-Transfer Mechanism 38
5.4 Analysis of Rate-Limiting Charge-Transfer Reactions 40
5.5 Temperature Dependence 41
6. Conclusions 43
6.1 Improvements 43
6.2 Future Direction 44
7. References 45
Distribution 49

FIGURES

Figure 1: Illustration of global reactions and basic operation in (a) electrolysis operation and (b) fuel cell operation. 10
Figure 2: SOEC diagram and processes (Image courtesy of Robert Kee) 10

Figure 3: Illustration of the cross-section of the patterned electrode cell used in the 17
Figure 4. Example of a Tafel plot result from Sukeshini experiments [12]. 19
Figure 5: SEM showing fracture cross-section of planar cell..... 21
Figure 6: Picture of completed planar and tubular SOCs. 22
Figure 7: SEM showing fracture cross-section of tubular SOC. 23
Figure 8: Photograph of electrical connections to the air electrode of a tubular cell. 24
Figure 9: Illustration of tubular solid-oxide electrolysis cell with current collection and voltage sense lines and ceramic mounting sleeves operating under cathodic polarization. (Image courtesy Robert Kee)..... 24
Figure 10: Process flow diagram of testing fixture..... 25
Figure 11: Picture of actual testing fixture. 26
Figure 12 (Left): Comparison of polarization characteristics between model and experimental measurements for H2-H_2O mixtures. The partial pressure of H_2O is fixed, with the varying H_2 partial pressure balanced by Ar. The system is isothermal at 850 °C and 0.83 atm. The cha charge-transfer model considers only the hydrogen-spillover mechanism..... 36
Figure 13 (Right): Comparison of polarization characteristics between model and experimental measurements for vH_2O case. The charge-transfer model considers only the hydrogen-spillover mechanism. 36
Figure 14 (Left): Comparison of polarization characteristics between model and experimental measurements for vCO case. The charge-transfer model considers only the hydrogen-spillover mechanism. 37
Figure 15 (Right): Comparison of polarization characteristics between model and experimental measurements for vCO2 case. The charge-transfer model considers only the hydrogen-spillover mechanism. 37
Figure 16 (Left): Comparison of polarization characteristics between model and experimental measurements for vH_2 case. The charge-transfer model considers only the oxygen-spillover mechanism. 38
Figure 17 (Right): Comparison of polarization characteristics between model and experimental measurements for vH2O case. The charge-transfer model considers only the oxygen-spillover mechanism. 38
Figure 18 (Left): Comparison of polarization characteristics between model and experimental measurements for vCO case. The charge-transfer model considers only the oxygen-spillover mechanism. 39
Figure 19 (Right) : Comparison of polarization characteristics between model and experimental measurements for vCO_2 case. The charge-transfer model considers only the oxygen-spillover mechanism. 39
Figure 20 (Left): Comparison of polarization characteristics between model and experimental measurements for vCO case. The charge-transfer model considers both the hydrogen- and oxygen-spillover mechanism. 40
Figure 21 (Right): Comparison of polarization characteristics between model and experimental measurements for vCO_2 case. The charge-transfer model considers both the hydrogen- and oxygen-spillover mechanism. 40
Figure 22: Comparison of the currents produced by each rate-limiting charge- transfer reaction step at A) 850 °C and B) 750 °C. The partial pressure of CO is fixed, and the varying CO_2 partial pressure is balance by Ar. The system is at 0.83 atm. 41

Figure 23: Comparison of polarization characteristics between model and experimental measurements for vCO2 case. The system is isothermal at 750 °C. The charge-transfer model considers both the hydrogen- and oxygen-spillover mechanism. 42
Figure 24: Current density as a function of temperature (Arrhenius form) for indicated operating condition. 42

TABLES

Table 1: Inlet fuel species composition (flow rates, sccm) 27
Table 2: Calculations for utilization in each test 27
Table 3: Parameters for modeling the MEA structure 30
Table 4: Heterogeneous reaction mechanism for methane reforming on a nickel. 32
Table 5: Heterogeneous reaction mechanism on a YSZ surface 32
Table 6: Hydrogen spillover charge-transfer pathway 33
Table 7: Oxygen spillover charge-transfer pathway 33
Table 8: Inlet fuel species composition (mole percent) 35

NOMENCLATURE

Cermet	Ceramic-Metallic
CFCC	Colorado Fuel Cell
CSM	Colorado School of Mines
CTE	Coefficient of Thermal Expansion
DGM	Dusty Gas Model
HTES	High Temperature Electrolysis of Steam
LSM	Strontium Doped Lanthanum Manganite
OCV	Open-Circuit Voltage
ScSZ	Scandia-Stabilized Zirconia
SNL	Sandia National Laboratories
SOC	Solid Oxide Cell
SOEC	Solid Oxide Electrolysis Cell
SOFC	Solid Oxide Fuel Cell
Syn gas	Synthesis Gas
TPB	Triple-Phase Boundary
WGS	Water Gas Shift
YSZ	Yttria-Stabilized Zirconia

1. INTRODUCTION

Solid-oxide electrochemical cells are an exciting new technology. Development of solid-oxide cells (SOCs) has advanced considerable in recent years and continues to progress rapidly. This thesis studies several aspects of SOCs and contributes useful information to their continued development.

1.1. Background

Solid-oxide electrochemical cells are devices that directly convert chemical energy into electricity (solid-oxide fuel cell, SOFC) or use electricity to drive an electrolysis reaction (solid-oxide electrolysis cell, SOEC). The principles behind SOFC and SOEC operation are very similar. Thus, they share many of the same advantages: high efficiency, solid state, simple scaling from high to low power, and relatively high gravimetric power densities [1]. While SOFCs convert chemical energy into electricity, SOECs do just the opposite and convert electrical energy into chemical energy.

In an SOEC, electricity is provided to the cell to electrochemically convert steam or carbon dioxide into hydrogen and carbon monoxide, respectively, as seen in Figure 1a. The solid-oxide cell is composed of three layers: the anode, electrolyte, and cathode. When functioning as an electrolysis cell, the fuel electrode is the cathode, where steam and CO_2 are electrochemically reduced to generate an oxygen ion (O^{2-}):

$$H_2O + 2e^- \rightarrow H_2 + O^{2-}$$
$$CO_2 + 2e^- \rightarrow CO + O^{2-}$$

In both cases, the oxygen ions are conducted through the electrolyte:

$$O^{2-} \rightarrow O + 2e^-$$

The extra electrons are stripped away and the oxygen atoms recombine to form molecular oxygen at the air electrode, or anode in electrolysis operation:

$$O + O \rightarrow O_2$$

These are global electrochemical reactions, however, and while accurately representing the net process, they do not accurately depict the sequence of elementary reactions involved. These global reactions are shown in their proper place graphically in Figure 1a. A solid-oxide cell operating as a fuel cell is shown in Figure 1b. The reactions are reversed and electricity is generated from the cell.

The idea of using a high temperature cell for electrolysis has been demonstrated previously. Isenberg presented the idea of using electrical energy and waste heat from power plants to operate such a cell as early as 1981 [2]. Results were presented for the electrolysis of both steam and carbon dioxide separately. Recently, renewed interest in energy storage through hydrogen

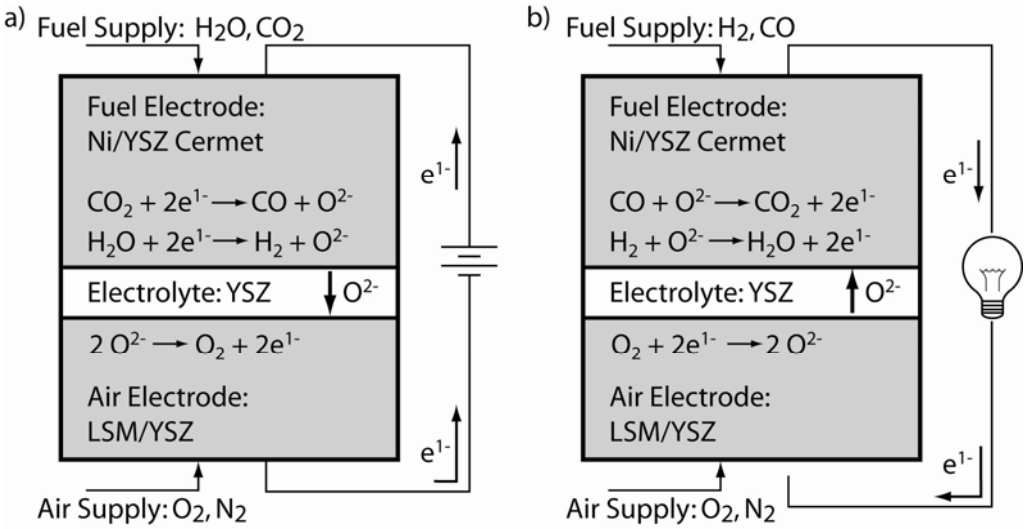

Figure 1: Illustration of global reactions and basic operation in (a) electrolysis operation and (b) fuel cell operation.

and syngas (synthesis gas, H_2 and CO) production has led to increased research into reversible SOFC and specific SOEC studies [3-6]. The production of high quality hydrogen as a means of energy storage for nuclear power has also recently been considered as a viable option [7].

In any solid-oxide cell (SOC) there are coupled and competing systems including but not limited to electrochemical charge-transfer reactions, gas transport, and thermal heterogeneous chemistry. A number of these processes are shown in Figure 2; gases are transported across each electrode to the electrolyte interface where electrochemical charge-transfer reactions are highlighted; heterogeneous chemistry is shown as a water-gas shift (WGS) reaction (globally, $CO + H_2O \leftrightarrow CO_2 + H_2$).

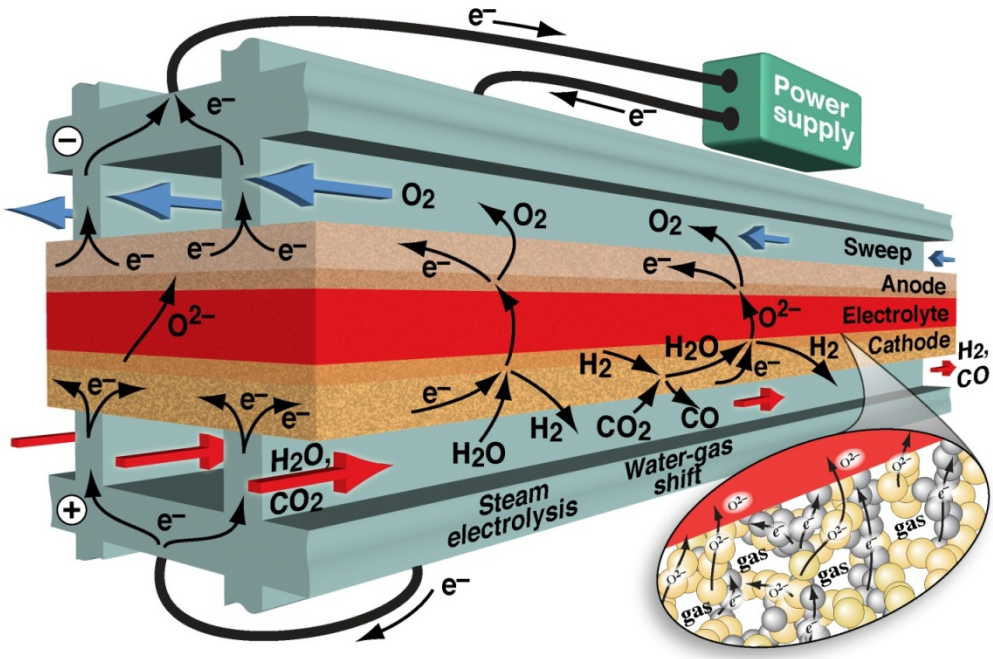

Figure 2: SOEC diagram and processes (Image courtesy of Robert Kee).

Electrochemical charge transfer reactions occur at so-called triple phase boundaries (TPBs) at the interface of the electrode (anode or cathode) and electrolyte; the electrochemically active regions typically only span 30 μm. Frequently, the cathode is composed of two layers: a cathode functional layer immediately next to the electrolyte and the bulk cathode. The functional layer is composed of relatively small particles and serves to increase the surface area of the TPB which, in turn, promotes the electrochemical charge transfer reactions. The cathode or cathode support has much higher porosity to aid in gas transport and often also provides mechanical support for the cell. The dense electrolyte separates the electrodes electronically and provides a pathway for ion transfer, specifically oxygen ions. This separation forces the electrons stripped off of oxygen ions in the anode to travel around an external circuit, instead of creating an electrical "short circuit" within the cell.

Much of the technology used in solid-oxide electrolysis cells matches or builds on that of solid-oxide fuel cells, particularly in the area of cell materials. Most of the materials selected for SOECs are those that have been in use in traditional SOFCs. Potential cathode materials include Ni-YSZ ceramic-metallic (cermet), samarium-doped ceria, and recently various LSCM (lanthanum strontium chromium manganite) doped perovskites [3, 8]. Anode materials considered are LSM (lanthanum strontium manganite), LSF (lanthanum strontium ferrite), or LSCo (lanthanum strontium cobaltite), all combined with the electrolyte material [9]. Possible electrolyte materials are YSZ (yttria stabilized zirconia), ScSZ (scandia stabilized zirconia), LSGM (lanthanum strontium gallium manganite), and GDC (gadolinium doped ceria) [3]. Material composition and selection used in this study are discussed in more depth in Chapter 3. Due to their availability and data available, the cells used in this study are composed of a Ni-YSZ cathode, YSZ electrolyte, and LSM anode. These materials are also the most commonly used by other fuel cell developers.

1.2 Motivation

A large body of research in solid-oxide fuel cells (SOFCs) has greatly advanced the fundamental understanding of high-temperature electrochemical processes. However, the coupled interactions of gas transport, heterogeneous thermal chemistry and electrochemical charge transfer are less well understood for high-temperature electrolysis. This study focuses on a series of experiments that generate key data from which rate coefficients can be established. The relative correlation to experimental data for the different pathways is then analyzed.

Previous work in elementary chemistry has been performed in steam electrolysis by Mizusaki, et al. with nickel patterned electrodes [10, 11]. Sukeshini, et al. have completed similar patterned electrode experiments with CO oxidation [12]. Both of these works have crafted reaction rates based on their experimental data; however, the idealized patterned cells do not incorporate gas transport and heterogeneous chemical reactions occurring throughout the electrode. This work will scale up the patterned electrode cell experiments to more practical working size cells; meaning the coupled interactions previously mentioned will have a role in the polarization behavior of the cell. Also, by scaling up to a larger active cell, results can be applied in a practical, commercial manner.

1.3 Approach

The electrochemical performance of tubular solid oxide cells is measured over a range of operating conditions. Model parameters, particularly charge-transfer reaction rates, are then varied to match model predictions to the experimental data set. In this manner, the importance of gas transport, thermal chemistry, and charge transfer can be contrasted intuitively. Both anodic and cathodic potentials are imposed during the tests so performance in both electrolysis and fuel-cell mode can be incorporated into the same model. It is important that the reaction mechanism match the data over the entire spectrum of operation, not just a single branch. This combined numerical and experimental study brings new insight to charge-transfer chemistry in high temperature solid oxide cells.

2. BACKGROUND

High temperature electrolysis of steam represents a viable path to hydrogen and syngas production to compete with other technologies. However, much work must be done to make SOECs economical and extend their life span. In this chapter, the principles of hydrogen or syngas production by electrolysis are reviewed, including cell materials, a discussion of cell degradation issues, and previous work on charge-transfer chemistry. Understanding these previous works is a large step in moving forward in SOEC technology.

2.1 Hydrogen/Syngas Production Options

Many industrial processes require the use of hydrogen or synthesis gas. Typically, hydrogen is produced through either steam reforming or partial oxidation of fossil fuels. This requires an initial desulfurization of the fuel to protect the catalyst used in the reformer and also further gas purification to remove remaining CO and CO2 after the water gas shift reaction (globally, $CO + H_2O \leftrightarrow CO_2 + H_2$) [13]. There are many steps involved in fossil-fuel-based hydrogen production and this process results in greenhouse-gas emissions.

Water electrolysis is another well-established method of hydrogen production. Water electrolysis basically involves splitting water into hydrogen and oxygen by passing a large, direct electrical current through deionized water that has been made more electrically conducting by the addition of hydrogen or hydroxyl ions (e.g. alkaline potassium hydroxide). Hydrogen production by water electrolysis requires initial purification followed by gas separation after the electrolyzer. Generally, the cost of water electrolysis is higher than that of fossil fuel reforming [13]. The overall hydrogen production efficiency is only around 27% using current methods [14].

Compared to low temperature water electrolysis, high-temperature (700-1000 °C) steam electrolysis via SOEC can be more efficient. High temperature electrolysis of steam (HTES) uses a combination of thermal energy and electricity to split water. From a thermodynamics and kinetics standpoint, the high temperatures can make activation over-potentials lower and increase the mobility of the oxygen ion [2, 14-16]. A feasible combined system efficiency of 46% at 850_C for HTES has been calculated previously [14]. In addition to the increase in efficiency, a high-temperature steam electrolysis system supported by a nuclear power plant is able to produce hydrogen without the greenhouse gas emissions associated with hydrocarbon processes, while also providing a means to store nuclear power [7].

Solid-oxide electrolysis cells can also be tailored to co-electrolyze H2O and CO2, providing valuable syngas (H_2 & CO) as the product. Synthesis gas is a basic building block for numerous chemical processes, including liquid fuel production via processes such as Fischer-Tropsch.

2.2 Materials Development

There are a wide range of materials available for use as electrodes and electrolytes in SOFCs today. Typically, the materials for solid oxide electrolysis cells have been limited to those used in solid oxide fuel cells, although some research into materials strictly for SOEC use has been

published [8, 9]. A material must be selected for each layer of the cell: the electrolyte, the fuel electrode, and the air electrode. These materials are reviewed in this section.

2.2.1. Electrolyte Materials

The electrolyte for a SOEC must be chemically stable and have high ionic conductivity at high operating temperatures. The electronic conductivity of the electrolyte must be low in order to prevent internal electrical short circuits. The presence of electronic conduction will lower efficiencies of the cell [4]. The layer must be thick and dense enough to eliminate any gas crossover between the fuel and air sides; however, a thinner electrolyte will cause less ohmic losses.

There are two classes of electrolyte materials: oxygen ion-conducting and proton-conducting. The most popular oxygen ion conductive electrolyte material is stabilized zirconia because of its well-known chemical stability and acceptable levels of ionic conductivity. The zirconia is most commonly stabilized with Y_2O_3 in various dopant levels although Yb_2O_3 and Sc_2O_3 are also used. Scandia-stabilized zirconia (ScSZ) has the highest conductivity of the three, but is not widely used, due to its high cost. By comparison, yttria-stabilized zirconia (YSZ) is much more economical and offers the best combination of ionic conductivity and stability [4]. These facts contribute to the widespread use of YSZ by cell developers.

Doped ceria is also a potential oxygen-ion-conductive electrolyte material. Gadolinia and samaria are the most commonly used dopants. Ceria electrolytes are primarily used at low temperatures (<550 °C). At high temperatures, cerates have a significant amount of electronic conductivity which decreases the performance of the cell. Ceria electrolytes also have a lower mechanical strength than stabilized zirconia [3].

Another set of possible oxygen-ion-conducting electrolyte materials is doped lanthanum gallates. Typically strontium and magnesium are doped on the lanthanum and gallium sites, respectively. The conductivity of $La_{0:9}Sr_{0:1}Ga_{0:8}Mg_{0:2}O_3$ (LSGM) was found to be higher than conventional YSZ and ScSZ at intermediate to high temperatures, however, there are several drawbacks to this set of materials as well; LSGM has a low mechanical strength, high cost of manufacture, and high reactivity with nickel, which is present in the electrode. At high temperatures, LSGM and Ni form lanthanum nickelates, leading to a significant loss in conductivity. This materials instability can, however, be overcome through the use of a ceria barrier layer [4, 17].

Proton-conducting electrolyte materials are far less commonly used as solid-oxide electrochemical cells. Most efforts in developing high-temperature proton conductors have been centered around perovskite-type materials with doped cerates, zirconates, and titanates. Of these, cerate-based perovskites are the most attractive because of the combination of high proton conductivity and good stability under fuel-cell operating conditions [4]. Typical substitutions for the A-site of the cerate are barium and strontium, producing $BaCeO_3$ and $SrCeO_3$. The orthorhombic structure of $SrCeO_3$ inhibits oxygen ion conduction but has little effect on proton conduction. Therefore, $SrCeO_3$ may be more suitable for steam-electrolysis applications. The perovskite- type cerates, however, react readily with H_2O and CO_2 and may not be suitable for co-electrolysis [3].

Yttria-stabilized zirconia has been chosen as the electrolyte material for the SOECs in this study due to its mechanical strength, decent conductivity, and widespread use.

2.2.1 Fuel Electrode

The fuel electrode in an SOEC must fufill several criteria. The electrode must be porous to enable sfficient gas transport between the fuel channel and the electrode- electrolyte interface, have high electrical conductivity to enable electrons to travel from the interconnects, display some measure of catalytic activity, and have a similar coefficient of thermal expansion (CTE) as the electrolyte to minimize thermal stresses. Also, it is beneficial for the electrode to be stable in a redox environment.

Noble metals, such as platinum and non-precious metals, such as nickel and cobalt, can be used for the fuel electrode in SOCs. Noble metals are generally not used because of their extreme cost. Also, volatile oxides can form over time at high temperatures [4]. Nickel has a high level of electrochemical and reforming reactivity, and is the most widely used material for SOFCs and SOECs. The electrolyte material (YSZ, typically) is usually combined with the nickel to create a ceramic-metallic combination, called a “cermet." This combination helps to match CTE and also extend the triple-phase boundary into the electrode. Concerns over Ni include low sulfur tolerance, tendency for carbon deposition at low steam-to-carbon ratios, and redox tolerance [3]. If the Ni is allowed to re-oxidize to NiO during operation, there is a large volume increase which can create large mechanical stresses within the cell.

Copper-based fuel electrodes are also being considered for use in both SOFCs and SOECs. Carbon deposition does not readily occur as it does with nickel, but copper has limited reactivity and a low melting point which can cause difficulties in fabrication. The copper is generally combined with ceria into a cermet for the same reasons as stated previously [3].

To combat redox and sulfur-tolerance issues, conducting ceramic electrodes are being researched. These are usually mixed ionic and electronic conducting perovskites. Recently, Yang and Irvine considered $(La_{0:75}Sr_{0:25})_{0:95}Mn_{0:5}Cr_{0:5}O_3$ (LSCM) as a fuel electrode for solid oxide electrolysis cells [8]. Improved performance compared to Ni-based electrodes was observed in low- or no-hydrogen conditions. However, in most operational conditions these conducting ceramics have relatively low catalytic activity and conductivity for efficient operation in comparison to Ni-YSZ-based SOCs [3].

A Ni-YSZ cermet electrode is being used for these tests, specifically a “reaction-sintered" Ni-YSZ cermet produced by CoorsTek, Inc. The reaction-sintered powders are significantly cheaper to produce and still have very good conductivity and mechanical strength [18]. More information on these materials is given in the Experimental section.

2.2.3 Air Electrode

The air electrode has mostly the same specifications as the fuel side (porous, electrically conductive), only instead of oxidizing fuels or reducing steam, the air electrode must provide sites for oxidant reduction or oxygen evolution ($O^{2-} + O^{2-} \rightarrow O_2 + 4e^-$).

Noble metals can also be used as the air electrode, but are usually not because of cost considerations. Also, a relatively weak interfacial bond is established between the electrolyte and noble metal, leading to problems with corrosion [3].

Electronically conducting mixed oxides compose the other classes of air electrode materials. These are made up of lanthanum manganites, cobaltites, and ferrites; each group includes a variety of doping species and dopant amounts. Doped $LaMnO_3$ has been used very extensively as a cathode material in SOFCs due to a high conductivity and adequate compatibility with electrolyte materials. A large number of dopants have been tested, and presently, strontium doping (LSM) is most commonly used [3]. It has been noted that during operation, MnOx may diffuse from the LSM into the YSZ, resulting in a reaction of La_2O_3 or SrO with YSZ to form poorly conducting $La_2Zr_2O_7$ or $SrZrO_3$ [4]. This problem can be solved through increasing manganite dopant levels.

Doped $LaCoO_3$ creates the lanthanum cobaltite group. Another perovskite, it is similar to LSM in structure and dopants available. Generally, the lanthanum cobaltites have a higher conductivity and catalytic activity than the lanthanum manganites, but tend to easily interact with YSZ to form insulating phases. They also have a relatively high CTE [4]. Lanthanum ferrites are also a perovskite group considered for air electrode use. The ferrites also generally have higher conductivity than LSM, but development has been limited to date.

For the cells used in this study, LSM is applied as an air electrode. Even though there are some problems reported, LSM is the most studied and used today; therefore, it is the most comparable with previous results. There is also a history of use of LSM in the Colorado Fuel Cell Center (CFCC) and the application methods and behavior of the material are well known.

2.3 Electrolysis Degradation

As previously stated, a solid oxide electrolysis cell offers many of the same strengths and weaknesses as a solid oxide fuel cell. However, it has been found that SOECs suffer from a vastly increased degradation rate. Long-term degradation rates have been found to be up to five times higher for SOECs compared to similar SOFC testing [19]. Hauch et al. found in degradation tests from 750 °C to 950 °C and current densities from -0.25 A/cm^2 to -0.5 A/cm^2 (negative sign indicating cathodic polarization) that cell passivation mainly occurred in the first 100 h of electrolysis operation, with less passivation noted at higher temperatures. Much of the degradation was attributed to migration of impurities from glass sealing [20]. In a follow-on publication, the glass seal was replaced with a gold foil and platinum paste seal to remove the possibility of silica impurities. A degradation rate of between 2%/1000 h and 5%/1000 h was noted in the absence of glass sealing. These rates are still higher than that of fuel-cell operation in similar cells. Analysis of electrochemical impedance spectra led the authors to believe that a majority of the degradation was caused by increased losses in the fuel electrode. A mechanism for this degradation was not suggested.
Post-mortem analysis revealed that the Ni particle size distribution had changed over the course of testing. In a high current density test sample, scanning electron microscopy (SEM) images show a dense Ni-YSZ layer of approximately 2-4 μm has formed at the fuel-electrode/electrolyte

interface. It is surmised that Ni has relocated and filled in the porosity of the first few microns of the electrode. This densification at the electrolyte interface was not seen in lower current density tests [21].

2.4 Charge-Transfer Chemistry

The experiments in this study have been inspired by previous work on charge-transfer chemistry, building upon patterned electrode experiments and modeling. These patterned electrode experiments are reviewed in this section.

2.4.1 Mizusaki Patterned Electrode Experiments

To improve fundamental understanding of charge-transfer chemistry, Mizusaki et al. created a unique fuel-cell geometry that attempted to eliminate competing fuel-cell processes to enable focus on the charge-transfer chemistry [11]. Mizusaki et al. created a stripe pattern of nickel on a single-crystal YSZ surface through photolithography techniques. In this way, the length of the triple phase boundary (TPB) per unit area was well defined and could be controlled by varying the width of the nickel strips and the width between each strip. A cross-section has been illustrated for reference in Figure 3. This architecture also minimized gas-transport limitations, to enable focus on the charge transfer. The dimensions reported in experimentation were 10 µm wide Ni strips separated by 25 µm of YSZ, creating a TPB length per unit area of 303 cm/cm^2. The experiments were operated under isothermal conditions at 700 °C. Fuel partial pressures were varied and a reaction mechanism for H_2-H_2O atmospheres at the anode of an SOFC was developed.

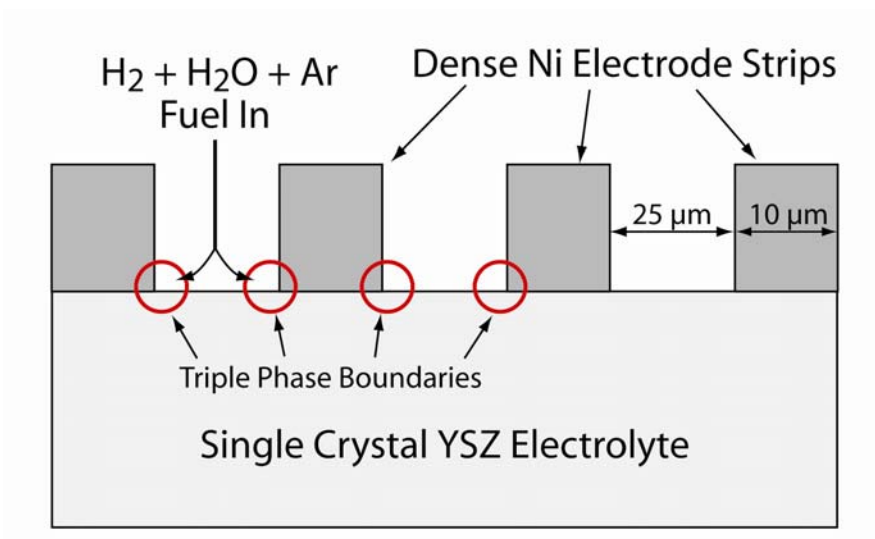

Figure 3: Illustration of the cross-section of the patterned electrode cell used in the

Mizusaki et al. determined that the rate of anodic reaction (fuel-cell operation) was essentially determined by the reaction of H_2(g) and the adsorbed oxygen on the nickel surface,

$H_2(g) + O(Ni) \rightarrow H_2O(Ni)$. The cathodic reaction (electrolysis operation) was found to be determined by the first-order reaction or surface-diffusion process of adsorbed hydrogen. This was assumed to take place through the following reaction sequence:

$$H_2O(g) \rightarrow H_2O_{ad} \rightarrow H_{ad} + OH_{ad}:$$

The experimental results were also explained by assuming a global charge transfer reaction

$$O^{2-}{}_O + (Ni) \leftrightarrow O(Ni) + V_O + 2e^-$$

is fast and remains close to equilibrium. In this equation, the "Ni" indicates the nickel surface and the "O" indicates an oxygen site on the YSZ surface. This charge transfer reaction predicts that oxygen ions from the YSZ readily cross the TPB and adsorb onto the nickel surface; this releases two electrons into the fuel-electrode bulk.

Although the data is widely used, the patterned cell tested in the experiment is not practical for actual use and the current densities are very small. Later studies have used data from the Mizusaki paper to further develop models for H_2-H_2O systems. The work herein will apply the same testing techniques to full size cells.

2.4.2 Sukeshini CO/H_2 Oxidation on Patterned Electrodes

Sukeshini et al. [12] have extended patterned anode work in dealing with H_2, CO, and CO/H_2 mixtures in electrochemical oxidation. A similar technique compared to Mizusaki was used to create non-porous Ni pattern electrodes of various linewidths on a dense single-crystal YSZ electrolyte disk. Various mixtures of CO, H_2, Ar, and H_2O are supplied to the cell and polarization curves are created. EIS data was also taken at open circuit voltage to analyze anodic activation losses. Experiments were performed at temperatures from 750 °C to 850 °C so that activation energies could be examined.

Tafel plots are used to analyze the polarization data by fitting a simplified Butler- Volmer equation (2.1) for large positive anodic overpotential (η_a>200 mV) and deriving effective exchange current densities, i^o, and anode exchange coefficients, α_a, for the electrochemical oxidation process. The Butler-Volmer equation is a method of calculating the cell current density based on reaction thermodynamics and the applied overvoltage.

$$i_{A,fit} = k_\infty \exp\left(\frac{-E_a}{RT}\right) \exp\left(\frac{\alpha_a \eta_a F}{RT}\right) \tag{2.1}$$

In the simplified Butler-Volmer equation, k_∞ and E_a are the effective rate constant at infinite T and the activation energy barrier, respectively, for i^o [12]. Figure 4 shows an example plot from the Sukeshini work. The data points represent experimental measurements, while the lines show the simplified Butler-Volmer equation match to the data for high anodic overpotentials [12].

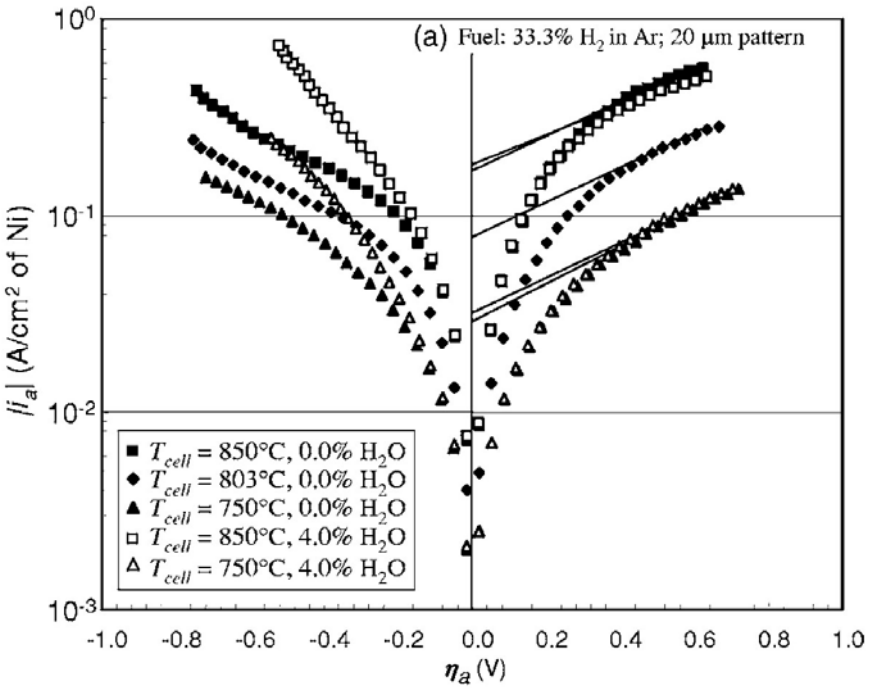

Figure 4. Example of a Tafel plot result from Sukeshini experiments [12].

Results at 850 °C show that the hydrogen system has very little activation losses while the dry CO exhibited a region of high activation η_a at low current density, i_a. However, as η_a increases past 400 mV, the slope of the polarization curve for CO approaches that of dry H_2. For 750 °C and 800 °C tests, α_a is very similar between the two fuels, as well. These similarities led Sukeshini et al. to believe the rate-controlling processes near the TPB may be comparable for CO and H_2.

There was a large drop in open-circuit voltage (OCV) for CO in the presence of H_2O (~4vol-% steam addition). The drop of approximately 0.4 V in OCV is not thought to be solely from thermodynamics. It is suggested that the water must inhibit the equilibration of CO electrochemical oxidation. The size of the drop in voltage η_a required to reach the ohmic loss region also increases. Overall the impact of H_2O on CO oxidation suggested to Sukeshini et al. that heterogeneous water-gas-shift reactions do not occur significantly near the TPB region because H_2-like behavior with wet CO feeds was not sustained.

For H_2 and CO mixtures, it was shown that for hydrogen content as low as 25% performance, was very similar to that of pure H_2. It appears that with an excess of hydrogen, carbon monoxide plays a very minimal role in the total electrochemical oxidation rate. Experiments were conducted where the CO was replaced with Ar to explore this further. Even substitution with inert gas had a negligible effect when excess H_2 is present. Because the hydrogen oxidation is so fast it does not appear that, under the test conditions in the Sukeshini paper, the water-gas-shift reaction or direct oxidation of CO has enough time to take place [12]. However, the lack of a porous electrode may be a large factor in this occurrence. Given a porous structure and presence of nickel catalyst, Sukeshini et al. thought the WGS reaction may have an effect.

2.4.3 Goodwin Electrochemical Oxidation Modeling

Goodwin et al. [22] have developed a model with various charge transfer mechanisms to further understand the data generated by the Mizusaki [10] and Sukeshini [12] efforts. Unlike most models, the Goodwin et al. model does not represent charge transfer in terms of activation overpotentials and the Butler-Volmer equation. The model developed in the Goodwin paper uses an elementary representation of the transport, chemistry, and electrochemistry in the vicinity of the TPB between gas-phase H_2, the Ni electrode, and the YSZ electrolyte [22]. The model attempts to match the data from the experiments by Mizusaki et al.

The model simultaneously incorporates surface-diffusive transport and nonfaradaic (i.e. catalytic) chemistry on the Ni and YSZ surfaces. Heterogeneous reaction pathways and thermal reactions are drawn from other literature. While the developed model can be used in many applications, Goodwin et al. attempted to evaluate two alternative charge-transfer pathways: an oxygen-spillover mechanism, where the rate-limiting step is the crossover of atomic oxygen from the YSZ surface to the Ni surface, and a hydrogen-spillover mechanism, where the crossing of an H atom from the Ni surface to the YSZ is rate limiting [22].

All chemical processes thermal and electrical are written as elementary reversible reactions represented through fundamental mass-action kinetics rates. The model built upon independent, published information about thermodynamic properties, thermal chemistry, and surface transport as much as possible so as to reduce the amount of variable parameters [22].

Immediately upon matching some DC polarization in Tafel form, Goodwin et al. notice that the anodic and cathodic symmetry factors, α_a and α_c, sum to approximately 2.5 (α_a = 1:8, α_c = 0:74), which is signi_cantly larger than the maximum value of 2 that would result from two elementary charge-transfer reactions in series. The data suggests at least two parallel charge-transfer pathways. The results show that the hydrogen-spillover mechanism represents the Mizusaki measurements very well, while the oxygen-spillover mechanism cannot represent the entire set of experiments [22].

The model developed by Goodwin et al. had a large amount of collaboration with the Colorado School of Mines. Because of the availability and in-depth understanding of this model locally, it has been extended to analyze the data generated by this study. A more in-depth look at the workings of this model will be taken later in this report.

3. EXPERIMENTAL METHOD

Tubular solid-oxide electrochemical cells are used for the experiments performed in this paper. The fuel electrode and electrolyte are fabricated at the CoorsTek, Inc. facility in Golden, CO, while the air electrode layers and current collection materials are applied at the Colorado Fuel Cell Center (CFCC). The testing fixture is specifically designed for SOC testing and has been improved in the course of previous cell testing. The metering of gases and water addition methods, as well as heat-up procedures are carefully recorded and designed to be as repeatable as possible.

3.1 Planar Cell Fabrication

An initial step into cell fabrication for this research was taken towards the fabrication of planar solid-oxide cells. The planar fuel-electrode supported SOCs were fabricated with a yttria-stabilized zirconia (YSZ) electrolyte, nickel-YSZ cermet fuel electrode, and strontium-doped lanthanum manganite (LSM) air electrode. A high-resolution micrograph of a planar cell is shown in Figure 5.

Cell fabrication begins with the fuel electrode, using a low-cost reaction-sintered NiO-YSZ material developed by CoorsTek, Inc. [18, 23]. The reaction-sintered powders (Ni-YRSZ) are a mixture of 65-wt% NiO, 32.2-wt% monoclinic zirconia, and 2.8 wt-% yttria powder, with associated binders. The nickel oxide enables the yttria-stabilization of the zirconia at significantly lower calcination temperatures than those required for stabilization in the absence of nickel. The result is that 8-mol% cubic-phase YSZ is formed from the monoclinic powders during the sintering process, significantly lowering materials and processing costs. Further details regarding this material are reported by Storjohann, et al. [18].

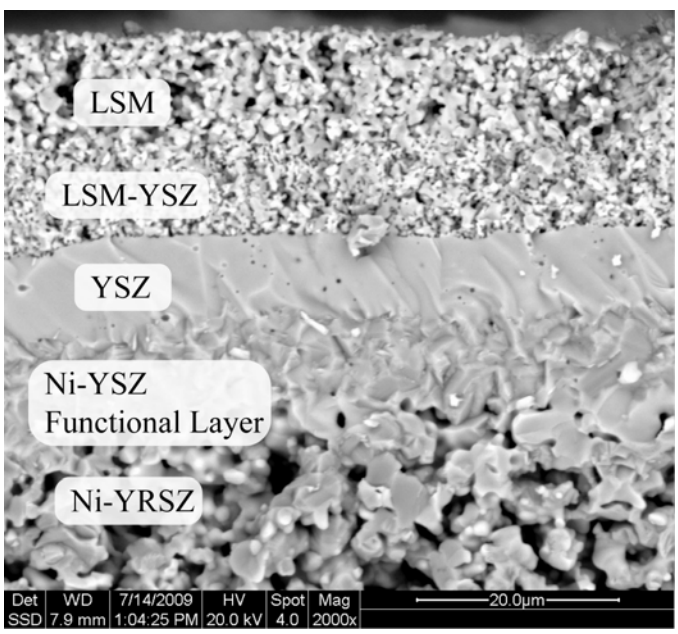

Figure 5: SEM showing fracture cross-section of planar cell.

Spray-dried NiO-YRSZ powders are weighed into 10-g portions and uniaxially pressed in a 5.72-cm-diameter (2.25 in) stainless-steel die using a uniaxial press loaded to 53.4 kN (12000 lbf) for a 10-s dwell time. The "green-state" fuel-electrode support is loaded into a holder and dip-coated in a NiO-YSZ slurry to create a fuel-electrode functional layer that is less porous and of a finer particle size than the support electrode. The functional-layer slurry is a mixture of 3 wt-% YSZ (Tosoh, TZ8Y), 5 wt-% NiO (Inco, Type F), 0.67 wt-% polyethyleneimine deocculant, 1.33 wt-% binder (Heraeus, V006), and 90 wt-% ethanol that has been ball milled for 24 hr using zirconia media. After drying, the electrolyte is applied to the green-state discs by dip-coating into a

YSZ-electrolyte slurry containing 12 wt-% YSZ (Tosoh, TZ8Y), 1 wt-% deocculant, 2 wt-% binder, and 85 wt-% ethanol. This electrolyte slurry is prepared by milling and stirring in the same fashion as the fuel-electrode functional-layer slurry. The dip-coating process for both the fuel-electrode functional layer and electrolyte consists of four separate three-second dips into the slurry. The planar cells are dipped in the same orientation each time and excess slurry is removed with a wetted paper wipe. This dipping method results in a layer that is approximately 10 µm thick, post-sintering.

After dip-coating both layers, the planar cells are placed onto YSZ-Al_2O_3 porous setter plates. An important subtlety in transferring the cell from the dip-coating holder to the setter plate is to orient the cell such that the downward facing surface during the dip coat is upward on the setter plate. The downward facing, diffusion-coated surface, results in a much more uniform layer that should avoid contact with the YSZ-Al_2O_3 plate during sintering. The cells are heated in a furnace to 300 °C with a 3-hr soak to vaporize the binders and other additives. The furnace temperature is then ramped to 1450 °C and held for three hours to co-sinter the layers.

After co-sintering, an air electrode functional layer is applied via screen printing. The electrode paste consists of a 50/50 wt-% mixture of strontium-doped lanthanum manganite ($(La_{0.8}Sr_{0.2})_{0.98}MnO_{3-x}$, LSM), 50 wt-% 8YSZ. For improved current collection, a pure LSM layer is applied over the functional layer. The air electrode is sintered in air at 1150 °C for 1.5 h, resulting in an air electrode thickness of approximately 20 µm. A completed planar cell can be seen in Figure 6 along with a tubular cell.

While many complete, working planar cells were fabricated during the course of this research, difficulties in reliably sealing and testing planar cells, as well as inconsistencies in the materials supplied, led to the use of tubular cells. The tubular geometry is much easier to create a gas-tight seal with, and controlled production from CoorsTek, Inc. led to fewer difficulties in fabrication.

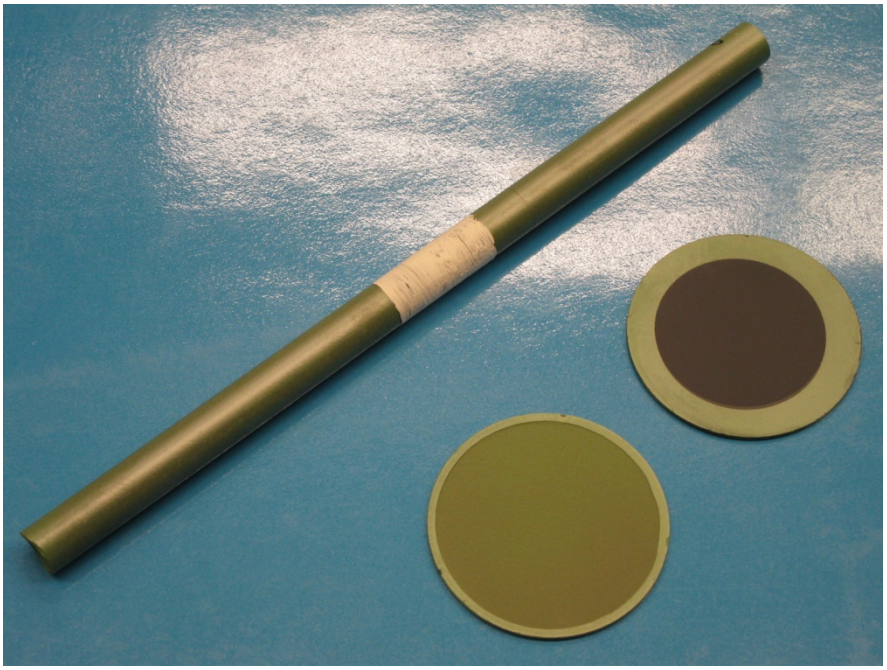

Figure 6: Picture of completed planar and tubular SOCs.

3.2 Tubular Cell Fabrication

The tubular fuel-electrode-supported SOECs fabricated for this study use the same materials as the developed planar cells: an yttria-stabilized zirconia (YSZ) electrolyte, nickel-YSZ cermet fuel electrode, and strontium-doped lanthanum manganite (LSM) air electrode. The same low-cost Ni-YRSZ powder [18] is used for the fuel electrode, however, now it is produced via extrusion; a dense electrolyte layer is then spray- coated onto the unfired “green-state" tube. The electrode and electrolyte are hang-fired and co-sintered at a temperature between 1400 °C and 1550 °C for 4 h, resulting in an electrolyte that is approximately 20 µm thick. The extruding process and electrolyte application are performed at the CoorsTek facility.

After co-sintering, an air-electrode functional layer is applied via roller printing at the Colorado Fuel Cell Center (CFCC). The electrode paste consists of a 50/50 wt-% mixture of strontium-doped lanthanum manganite ($(La_{0.8}Sr_{0.2})_{0.98}MnO_{3-x}$, LSM), 50 wt-% 8YSZ. Similar to the planar cells, a pure LSM layer is applied over the functional layer for improved current collection. The air electrode is sintered in air at 1200 °C for 1 h, resulting in an air electrode thickness of approximately 30 µm. All of the applied layers can be seen in SEM image in Figure 7.

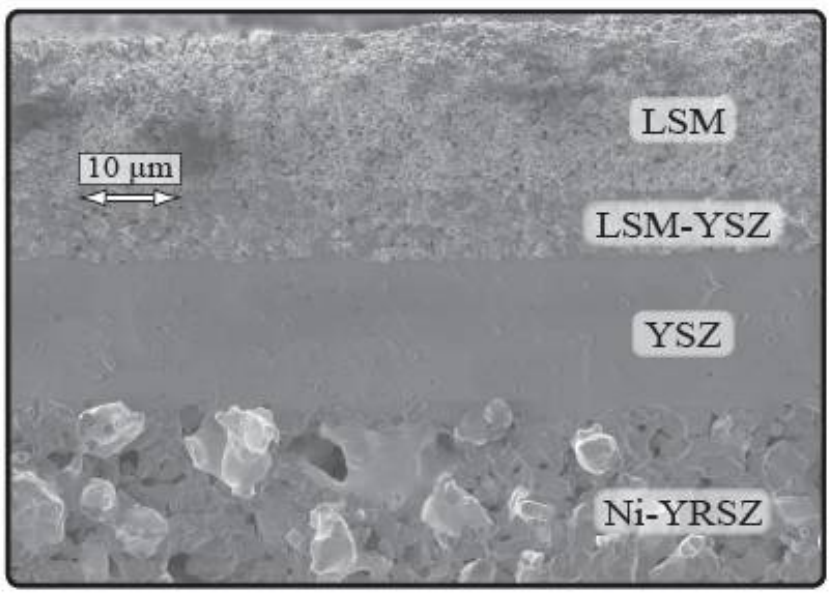

Figure 7: SEM showing fracture cross-section of tubular SOC.

The completed tubular cell, shown in Figure 6, has an outer diameter of approximately 9.8 mm and length of 180 mm. The air electrode is only applied a smaller, 25 mm active length. This yields an active area of roughly 7.5 cm2. Scanning electron microscopy images show a relatively high porosity (~ 42%) after reduction of the NiO to Ni.

3.3 Electrochemical Performance Measurements

Four wire leads are attached to the cell prior to testing. Two are connected to the fuel electrode with a nickel mesh, and two are connected to the air electrode with a wound silver wire on top of silver paste. One lead for each electrode is used for applying an electrical load to the cell, while the other only measures voltage. This is called the four-point probe technique. Because all of the

current is delivered through another wire, the four-point probe technique allows measurement of the cell potential without any ohmic losses from the voltage sensing wires. A load/source is applied and polarization is measured with the Chroma 63103 electronic load box. The current collection and sense leads for the air electrode are shown pictorially in Figure 8, and the electrical connection illustrated in entirety in Figure 9.

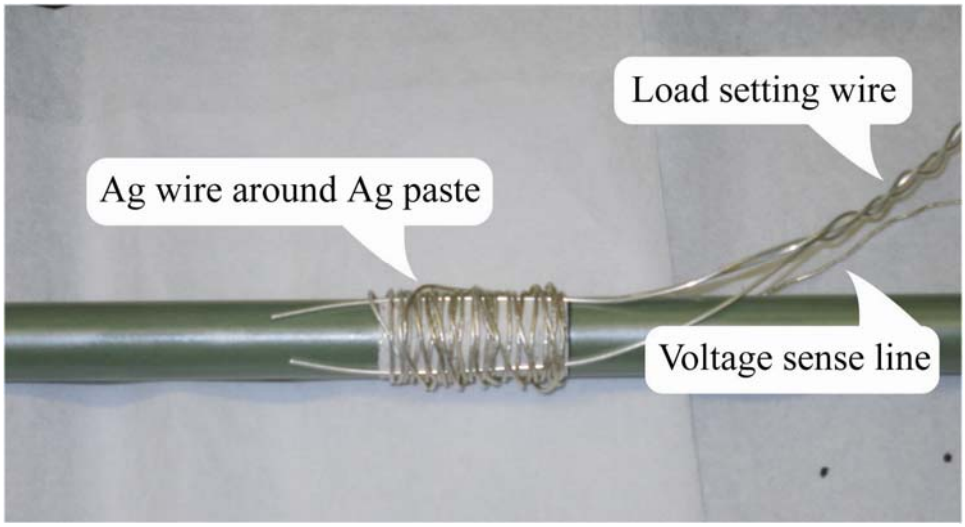

Figure 8: Photograph of electrical connections to the air electrode of a tubular cell.

The ends of the cell are sealed in alumina (Al_2O_3) sleeves with high temperature ceramic adhesive as shown in Figure 9. The ceramic tubes are then attached to a gas supply outside of the hot zone. The alumina is able to relieve any stresses associated with improper alignment of the cell and furnace and separates the furnace wall from contact with the cell.

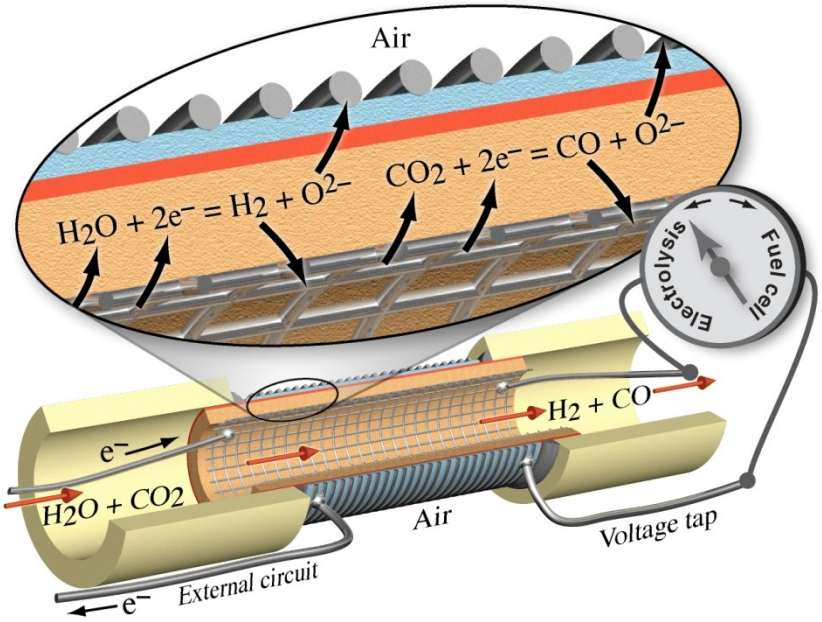

Figure 9: Illustration of tubular solid-oxide electrolysis cell with current collection and voltage sense lines and ceramic mounting sleeves operating under cathodic polarization. (Image courtesy Robert Kee)

The cell is heated to operational temperature in a split tube furnace (Applied Test Systems, Inc., Series 3210). Fuel is supplied to the cell through calibrated mass flow controllers (Alicat Scientific). The air electrode is simply exposed to ambient air within the furnace. Steam addition is accomplished through the use of an industrial nebulizer spraying into a heated 300 mL sample cylinder. The water flow rate is controlled with a Milligat pump (Global FIA), and all water is assumed to be vaporized. This assumption has been confirmed previously through use of a Rotronic HygroFlex2 humidity sensor, in addition to comparison of open circuit voltages to thermodynamically predicted values. All gas lines are stainless steel and all lines downstream of the water vaporizer are heated with Omega heat ropes to prevent condensation. A Chroma 63103 electronic load box is used to apply a load to the cell and record polarization data. The layout is illustrated in Figure 10 and Figure 11.

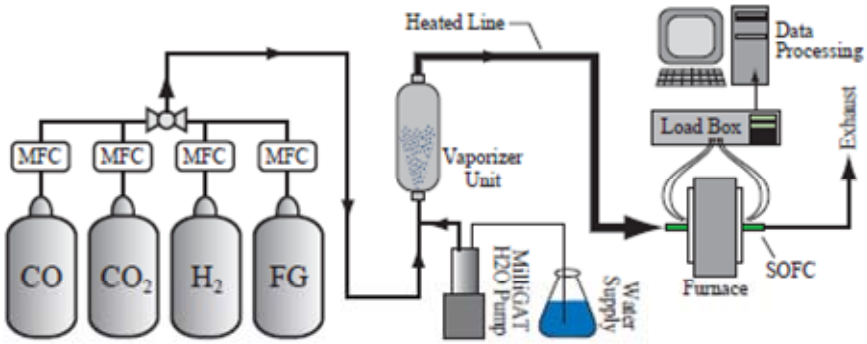

Figure 10: Process flow diagram of testing fixture.

Once the cell is secured in the test stand, the temperature is raised at 30 °C h^{-1} to operating conditions. During the heat-up period, 100 sccm of forming gas (3.5% H_2, balance Ar) is supplied to the fuel electrode to begin reducing the NiO to Ni. After reaching the desired operating temperature, the supply of forming gas is increased to 300 sccm to further reduce the NiO. Several hours later, the gas supply is gradually switched to 300 sccm hydrogen.

Once the voltage reaches the thermodynamically predicted open-circuit value, a sequentially increasing load is applied until it is determined that the NiO in the fuel electrode is fully reduced to Ni (no recovery after voltage drop upon increase in loading). At this point, gas flows required for a specific experiment are supplied to the cell and conditions are allowed to equilibrate for several hours. Polarization data is taken by supplying/drawing a constant current to/from the cell and recording the voltage. The cell is allowed to stabilize for 5 to 10 minutes at each current set point before recording the polarization data. Following each test sequence (i.e., gas composition), 300 sccm of hydrogen is supplied to the cell for at least 15 minutes to allow for recovery before initiating another test sequence.

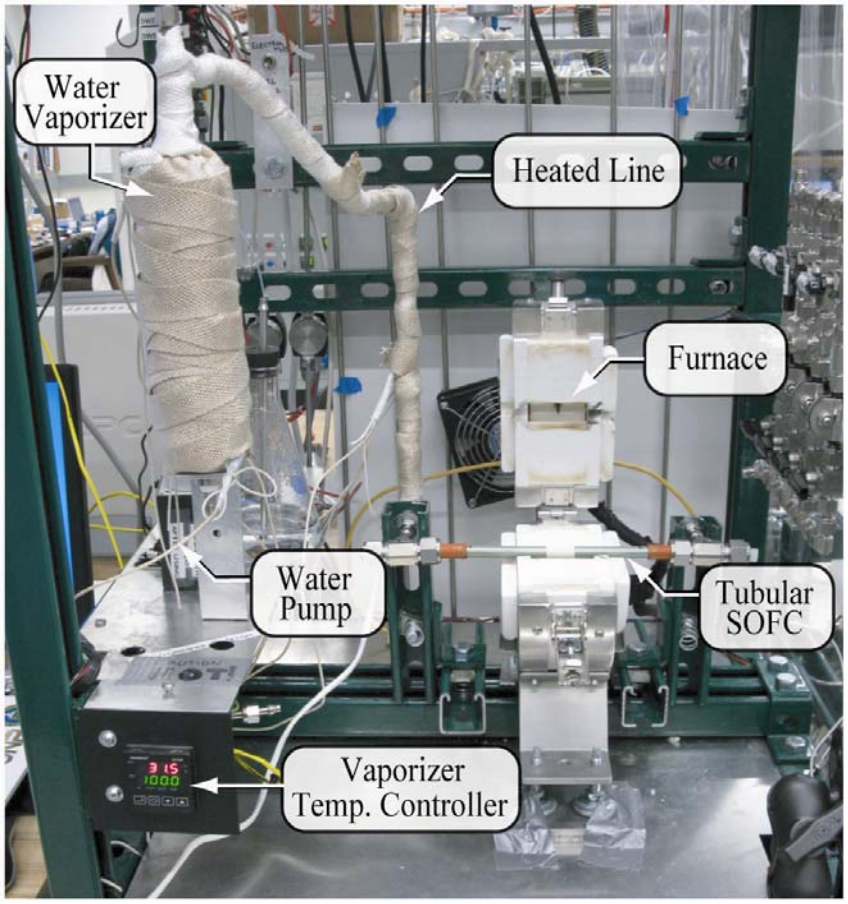

Figure 11: Picture of actual testing fixture.

3.4 Gas Flow Rates and Utilization

Careful thought was given to the construction of a matrix of gas compositions for experimentation. As will be explained in Chapter 4, Physical and Chemical Model, the fuel utilization during experimentation must remain fairly low, so as to not incur losses in cell performance and ensure a pseudo-one-dimensional modeling environment. One solution would be to supply an extremely large total fuel flow rate; however, flow rates also had to be designed around limitations in equipment. It was determined that a total flow rate of 400 sccm of fuel would allow for the largest spread in fuel compositions while staying within the performance limitations of the mass flow controllers available. Individual gas compositions were then calculated within this limit as shown in Table 1.

For each gas varied, the low-concentration set point was fixed to keep the maximum utilization at a fairly low value. The calculation of utilization is as follows:

$$\dot{n_{H2}} = \frac{i}{nF} \tag{3.1}$$

where n is the hydrogen consumption in mol/sec, i is the applied current, n is the number of electrons transferred in hydrogen oxidation, and F is Faraday's constant. The amount of H_2

consumed can be converted to a flow rate through ideal gas law; assuming standard temperature and pressure, a mole of gas fills 22.4 L. Multiplying this by n yields units of [L/sec]. The number can then easily be converted to a standard cubic centimeters per minute (sccm):

$$\left[\frac{mol}{sec}\right]\left[\frac{22.4L}{mol}\right]\left[\frac{60\ sec}{min}\right]\left[\frac{1000\ cm3}{L}\right] = [sccm]$$

Table 1: Inlet fuel species composition (flow rates, sccm)

Case	H_2	H_2O	CO_2	CO	Ar
vH2	236.9	79.0			84.2
(vary H_2)	142.1	79.0			178.9
	47.4	79.0			273.7
vH2O	98.7	236.9			64.4
(vary H_2O)	98.7	98.7			202.6
	98.7	39.5			261.8
vCO2	39.5	19.7	197.4	79.0	64.4
(vary CO_2)	39.5	19.7	98.7	79.0	163.1
	39.5	19.7	39.5	79.0	222.4
vCO	39.5	19.7	79.0	197.4	64.4
(vary CO)	39.5	19.7	79.0	98.7	163.1
	39.5	19.7	79.0	39.5	222.4

It was assumed initially that the highest current applied to the cell would be 4.5 A. The utilization was calculated for the hydrogen/steam system at each gas composition for this worst case scenario. The results of this calculation are given in Table 2.

Table 2: Calculations for utilization in each test

Case	H_2 Supplied (sccm)	Utilization i=4.5 A	Largest Applied Current (A)	H_2 Consumed (sccm)	Highest Utilization
vH2	236.9	13.23%	4.16	28.97	12.23%
(vary H_2)	142.1	22.05%	3.78	26.32	18.52%
	47.4	66.17%	3.33	23.19	48.96%
vH2O	98.7	31.76%	3.78	26.32	26.68%
(vary H_2O)	98.7	31.76%	4.15	28.90	29.29%
	98.7	31.76%	4.08	28.41	28.79%

While the utilization appears to be very high in the worst-case scenario for lastvH_2 composition, it was known that the performance would drop with lower amounts of H2 and a current of 4.5 A was fairly unreasonable. The actual highest applied current was found after testing and the highest level of utilization calculated. This is also given in Table 2. The data shows that the utilization is below 30% in almost all cases. Also, no concentration losses can be seen explicitly in the polarization data.

Utilization losses are thus assumed to have minimal role in lowered performance of the cell. Utilization numbers were not run for the co-electrolysis gas compositions. This is because other chemistry is involved in the cell and the amount of fuel actually delivered is uncertain. Because of this, similar flow rates used for hydrogen and steam were applied to CO and CO_2 and the utilization of these gases assumed to be similar.

4. COMPUTATIONAL MODEL

The model used in this experiment is based on that developed by Goodwin et al. It has been adjusted slightly to change pairs of irreversible reactions into reversible elementary reactions for this experiment by Dr. Huayang Zhu and Dr. Robert Kee, engineering faculty at the Colorado School of Mines. The model was implemented and matched to this experimental data by Dr. Zhu. Most of the detailed workings of the model are given elsewhere [22], so only an overview is supplied here.

4.1 Overview

High flow rates are used in experimentation such that the fluid residence time through the active portion of the tubular cell is very short. Because of this, fuel utilization is low and the flow channel composition is assumed to be constant. Due to the limited variability in conditions along the length of the tube, the model must only take into account radial variations though the thickness of the cell. This reduction to a one-dimensional computational environment simplifies the model significantly, although flooded conditions must be maintained experimentally.

Gaseous species transport through the porous electrode microstructure is represented by the Dusty-Gas Model (DGM) [24]. The DGM takes into account species fluxes due to ordinary diffusion, Knudsen diffusion, and Darcy flow driven by gradients of species concentrations and pressure [25]. Charge transport is represented using continuum differential equations that describe the electric potentials for the electrode and electrolyte phases as well as Faradaic charge transfer between phases [26]. Percolation theory is used to estimate the effective transport properties and triple-phase boundary (TPB) length of the percolated electronic and ionic-conducting electric phases [27]. Heterogeneous catalytic chemistry and charge-transfer chemistry within the electrodes is based upon elementary reaction mechanisms [22, 25]. The details of the model framework, including charge conservation equations, porous-media transport equations, and chemical kinetics equations are detailed elsewhere [22] and are not included in this report.

The model is adjusted to match the experimental data by altering parameters in the various charge-transfer reaction pathways. The adjusted parameters are the pre-exponential factor, the activation energy, and the anodic symmetry factor.

Non-adjustable parameters input to the model include the physical parameters individual to each material. However, the model results may give valuable insight into how to best adjust the material parameters for best performance. A list of the material properties is shown in Table 3.

The chemistry on the air electrode is taken from previous studies [25, 26]. Table 3 indicates parameters for the air-side charge-transfer kinetics in Butler-Volmer form.

Table 3: Parameters for modeling the MEA structure

Parameters	Value	Units
Fuel-electrode (fuel-cell anode)		
Thickness (L_a)	1000	μm
Porosity (ϕ_g)	0.40	
Ni volume fraction (Φ_{Ni})	0.30	
YSZ volume fraction (Φ_{YSZ})	0.30	
Tortuosity (τ_g)	2.30	
Pore radius (r_p)	0.90	μm
Ni particle radius (r_{Ni})	1.35	μm
YSZ particle radius (r_{YSZ})	1.35	μm
Specific catalyst area (A_s)	5.00E2	cm^{-1}
Specific TPB length (λ^V_{TPB})	1.50E8	cm^{-2}
Ni conductivity (σ_{Ni})	3.27E4 - 10.65(T)	S cm^{-1}
Air-electrode functional layer (fuel-cell cathode)		
Thickness (L_c)	10	μm
Porosity (ϕ_g)	0.20	
LSM volume fraction (Φ_{LSM})	0.39	
YSZ volume fraction (Φ_{YSZ})	0.41	
Tortuosity (τ_g)	5.40	
Pore radius (r_p)	0.20	μm
LSM particle radius (r_{LSM})	0.30	μm
YSZ particle radius (r_{YSZ})	0.30	μm
Exchange current factor (i^*_{ref,O_2})	1.17E2	A/cm^3
Activation energy (E_{a,O_2})	120.0	kJ/mol
Reference temperature (T_{ref})	750, 800, 850	°C
Anodic symmetry factor (α_a)	0.55	
Cathodic symmetry factor (α_c)	0.45	
LSM conductivity ($\sigma_{LSM} = \sigma^0_{LSM} T^{-1} \exp(-E_a/RT)$)		
σ^0_{LSM}	8.86E5	S cm^{-1}
E_a	9	kJ mol^{-1}
Air-electrode diffusion layer (fuel-cell cathode)		
Thickness (L_c)	20	μm
Porosity (ϕ_g)	0.35	
LSM volume fraction (Φ_{LSM})	0.65	
Tortuosity (τ_g)	4.00	
Pore radius (r_p)	0.40	μm
LSM particle radius (r_{LSM})	0.50	μm
YSZ Electrolyte		
Thickness (L_{el})	20	μm
Ion conductivity ($\sigma_{YSZ} = \sigma^0_{YSZ} T^{-1} \exp(-E_a/RT)$)		
σ_0	3.60E5	S cm^{-1}
E_a	80	kJ mol^{-1}

4.2 Reaction and Charge-Transfer Mechanisms

There are many reactions that occur during fuel cell or electrolysis operation in a SOC; the order of these reactions and speed at which they occur is part of the focus of this research. However, there are well-known global reactions that can be used to represent the net chemical reactions. While they provide little insight into cell optimization, understanding these global reactions helps to explain the operation of the cell in a broad sense.

Steam and carbon dioxide may either be consumed or produced electrochemically at the TPBs between the fuel electrode and the electrolyte. These half-cell processes can be represented in a global sense by reversible charge-transfer reactions as

$$H_2(g) + O^{2-}(e) \leftrightarrow H_2O(g) + 2e^-(f);$$
$$CO(g) + O^{2-}(e) \leftrightarrow CO_2(g) + 2e^-(f):$$

Reaction in the forward direction, as written, indicates operation as a fuel cell. Hydrogen and carbon monoxide fuels are electro-oxidized by oxygen ions. The phases are indicated as “g" for gas phase, “e" for the electrolyte phase and “f" for the fuel-electrode phase. Operation in the reverse directions represents electrolysis.

On the air electrode, molecular oxygen is electrochemically reduced at the boundary between the LSM and YSZ phases. This half-cell reaction can be written as

$$\tfrac{1}{2}\, O_2(g) + 2e^-(a) \leftrightarrow O^{2-}(e):$$

The air electrode phase is represented by “(a)". It is important to note that the terminology between fuel cell and electrolysis is reversed. The Ni/YSZ cermet electrode acts as the anode in fuel-cell operation and the cathode in electrolysis. Similarly, the LSM/YSZ electrode is the cathode when the SOC is operated as a fuel cell and anode as an electrolyzer. To avoid confusion, the terms `fuel electrode' and `air electrode will be used as much as possible in place of anode and cathode, as these terms will always apply to the same side.

Combining the half-cell reactions, the global reactions for H_2 and CO oxidation can be written as,

$$H2(g) + \tfrac{1}{2}\, O_2(g) \leftrightarrow H_2O(g);$$
$$CO(g) + \tfrac{1}{2}\, O_2(g) \leftrightarrow CO_2(g):$$

Again, the forward direction as written is in the fuel-cell direction; this can also be called anodic polarization. The electrolysis direction is the reverse of the reactions and is also indicated as cathodic polarization.

The global and half-cell reactions illustrate that in fuel-cell operation, fuel and oxygen are required to produce water and electricity. In electrolysis operation, steam or CO_2 and electricity are required to produce fuel. With basic understanding established, the approach in the rest of this paper is to represent all of the chemical and electrochemical processes as sequences of elementary reactions.

The thermal heterogeneous catalytic chemistry within the fuel electrode shows some of these elementary reactions occurring on the Ni surface. Table 4 shows the Ni-surface chemistry and is based on previously established mechanisms created for methane reforming over a Ni catalyst [25, 28, 29]. In the mechanism, “(g)” means the species is in the gas phase and “(Ni)” indicates the species is adsorbed onto the Ni surface. The thermal chemistry has been altered from its

original form to be represented as reversible reactions with self-consistent thermodynamic properties for all species rather than pairs of irreversible reactions.

Table 4: Heterogeneous reaction mechanism for methane reforming on a nickel.

	Reaction	A^* or γ_0 (mol, cm, s)	n or β	E (kJ/mol)
1	$H_2(g) + 2(Ni) \rightleftharpoons 2H(Ni)$	$0.01^\dagger$	0.0	0.0
2	$H_2O(g) + (Ni) \rightleftharpoons H_2O(Ni)$	$0.10^\dagger$	0.0	0.0
3	$H(Ni) + O(Ni) \rightleftharpoons OH(Ni) + (Ni)$	5.0×10^{22}	0.0	97.9
4	$H(Ni) + OH(Ni) \rightleftharpoons H_2O(Ni) + (Ni)$	3.0×10^{20}	0.0	42.7
5	$2OH(Ni) \rightleftharpoons H_2O(Ni) + O(Ni)$	3.0×10^{21}	0.0	100.0
6	$CO(g) + (Ni) \rightleftharpoons CO(Ni)$	$0.50^\dagger$	0.0	0.0
7	$CO_2(g) + (Ni) \rightleftharpoons CO_2(Ni)$	$1.0 \times 10^{-5\dagger}$	0.0	0.0
8	$C(Ni) + O(Ni) \rightleftharpoons CO(Ni)$	5.2×10^{23}	0.0	148.1
9	$CO(Ni) + O(Ni) \rightleftharpoons CO_2(Ni) + (Ni)$	3.0×10^{20}	0.0	42.7
10	$CH_4(g) + Ni(Ni) \rightleftharpoons CH_4(Ni)$	8.0×10^{-3}	0.0	0.0
11	$H(Ni) + CO(Ni) \rightleftharpoons (Ni) + HCO(Ni)$	4.019×10^{20}	-1.0	132.2
12	$(Ni) + HCO(Ni) \rightleftharpoons CH(Ni) + O(Ni)$	3.7×10^{24}	-3.0	95.8
13	$(Ni) + CH_4(Ni) \rightleftharpoons H(Ni) + CH3(Ni)$	3.7×10^{21}	0.0	57.7
14	$(Ni) + CH_3(Ni) \rightleftharpoons H(Ni) + CH2(Ni)$	3.7×10^{24}	0.0	100.0
15	$(Ni) + CH_2(Ni) \rightleftharpoons H(Ni) + CH(Ni)$	3.7×10^{24}	0.0	97.1
16	$(Ni) + CH(Ni) \rightleftharpoons H(Ni) + C(Ni)$	3.7×10^{21}	0.0	18.8
17	$CH_4(Ni) + O(Ni) \rightleftharpoons OH(Ni) + CH3(Ni)$	1.7×10^{24}	0.0	88.3
18	$CH_3(Ni) + O(Ni) \rightleftharpoons OH(Ni) + CH2(Ni)$	3.7×10^{24}	0.0	130.1
19	$CH_2(Ni) + O(Ni) \rightleftharpoons OH(Ni) + CH(Ni)$	3.7×10^{24}	0.0	126.8
20	$CH(Ni) + O(Ni) \rightleftharpoons OH(Ni) + C(Ni)$	3.7×10^{21}	0.0	48.1

* The forward rate coefficients are given in Arrhenius form as $k = AT^\beta \exp(-E/RT)$.
† Sticking coefficient in form of $\gamma = \gamma_0 T^n \exp(-E/RT)$. The sticking coefficient is dimensionless.
The available site density is $\Gamma = 1.7 \times 10^{-9}$ mol/cm^2.

The chemistry for the YSZ surface seen in Table 5 is taken from Goodwin et al. [22]. This mechanism assumes that only hydrogen and oxygen react on the YSZ surface. All carbon-containing species only react on the Ni. The YSZ surface is thought to have two different types of sites available: the Zr site and the χ site. The Zr site is a zirconium atom that is on the YSZ surface. The χ site is the site that is occupied by an oxygen ion as it emerges from the bulk YSZ to the surface. The oxygen-containing species on the χ site (O^{2-}, O^-, or OH^-) is thought to have a large effect on charge-transfer chemistry.

Table 5: Heterogeneous reaction mechanism on a YSZ surface

	Reaction	A^* or γ_0 (mol, cm, s)	E (kJ/mol)
1	$O_O^{2-} + (\chi) \rightleftharpoons O^{2-}(\chi) + V_O$	7.3×10^{12}	80.1
2	$H_2O(g) + (Zr) + O^{2-}(\chi) \rightleftharpoons OH^-(Zr) + OH^-(\chi)$	$1.2 \times 10^{-4\dagger}$	86.8
3	$OH^-(\chi) + (Zr) \rightleftharpoons OH^-(Zr) + (\chi)$	2.0×10^{10}	0.0
4	$H_2(g) + (Zr) + O^{2-}(\chi) \rightleftharpoons H^-(Zr) + OH^-(\chi)$	$1.0 \times 10^{-8\dagger}$	20.0

* The forward rate coefficients are given in Arrhenius form as $k = A\exp(-E/RT)$.
† Sticking coefficient in form of $\gamma = \gamma_0 \exp(-E/RT)$. The sticking coefficient is dimensionless.
The available site density for the (Zr) sites and (χ) sites is $\Gamma = 1.25 \times 10^{-9}$ mol/cm^2.

Two charge-transfer mechanisms are considered within the fuel electrode. The hydrogen-spillover mechanism (Table 6) assumes that adsorbed H on the Ni surface "spills over" to react with charged oxygen-containing species on the YSZ surface [22]. The first reaction, transferring H to the oxygen ion on the χ site, is thought to be very fast and the second reaction where steam is formed is thought to be rate limiting. As shown, the H2O is formed on the Ni surface and then desorbs. However, it is equally likely that the H2O is formed on the YSZ surface and desorbs from the χ site. In either case, the desorption occurs quickly and thus, results are largely unaffected.

Table 6: Hydrogen spillover charge-transfer pathway

	Reaction	A^* (mol, cm, s)	E (kJ/mol)	β_a
1	$H(Ni) + O^{2-}(\chi) \rightleftharpoons OH^-(\chi) + (Ni) + e^-$	1.00×10^{15}	50.0	0.500
2	$H(Ni) + OH^-(\chi) \rightleftharpoons H_2O(Ni) + (\chi) + e^-$	1.00×10^{13}	50.0	0.300

Alternatively, the oxygen-spillover mechanism (Table 7) assumes that the oxygen on the χ site on the YSZ surface spills over to the Ni surface. The first reaction only transfers an electron and is fast. The second reaction transfers both an atomic oxygen and a charge and is assumed to be rate-limiting. It is also possible for both of these charge-transfer mechanisms to be working in parallel. That is, both are occurring at the same time, although they may be at different rates.

Table 7: Oxygen spillover charge-transfer pathway

	Reaction	A^* (mol, cm, s)	E (kJ/mol)	β_a
1	$O^{2-}(\chi) \rightleftharpoons O^-(\chi) + e^-$	1.00×10^{8}	50.0	0.500
2	$O^-(\chi) + (Ni) \rightleftharpoons O(Ni) + (\chi) + e^-$	6.00×10^{11}	50.0	0.600

Table 6 and Table 7 already show the values used as the best fit across all operating conditions.

As will be shown in the results section, for a strictly H_2-H_2O system, the hydrogen-spillover mechanism provides a better fit to measurements than the oxygen-spillover mechanism. The addition of CO and CO_2 to the system can change this, as both CO and CO_2 are readily adsorbed on to the Ni surface and are unlikely to spill over to the YSZ surface sites.

5. RESULTS AND ANALYSIS

A set of experiments have been designed to assist in developing and validating the reaction chemistry for high temperature solid oxide electrolysis cells operating with mixtures of H_2, H_2O, CO, and CO_2. Understanding how the species partial pressures (i.e., reaction orders) influence the overall chemical kinetics is important in establishing the reaction chemistry. The general method is motivated by previous work on pattern-anode experiments by Mizusaki, et al. who studied hydrogen charge-transfer in patterned anode experiments [11]. A previously developed one-dimensional model has been used to examine rate parameters and match experimental data over a voltage range of E_{cell} = 0.4 V to E_{cell} = 1.4 V. Operation between open-circuit voltage (OCV) and E_{cell} = 0.4 V oxidizes the cell (fuel cell operation), while polarization between OCV and E_{cell} = 1.4 V reduces H_2O and CO_2 (electrolysis operation). The model incorporates electrochemical charge-transfer with hydrogen spillover (Table 6) and oxygen spillover (Table 7) reactions which can be implemented separately or in parallel.

Four sets of fuel-side gas compositions are used, varying H_2, H_2O, CO, and CO_2 individually at various operating temperatures: 750, 800, and 850 °C. For each operating temperature, there are three partial pressure set points for each varied fuel gas. The experimental operating pressure is 0.83 atm, which is the atmospheric pressure in Denver, CO, USA. Argon is used to maintain the constant partial pressures of the gases while one is varied. The complete matrix of tests is shown as flow rates in Table 1 and as percentages in Table 8. As an example, for the vH2 case, the hydrogen gas partial pressure is first held at a high gas-phase partial pressure. After experimentation at the first condition is complete, the H_2 partial pressure is lowered while the steam partial pressure is held constant by replacing the lost H_2 with Ar. This method is repeated again for a yet lower H_2 partial pressure and then applied to the other gas species.

Table 8: Inlet fuel species composition (mole percent)

Case	H_2	H_2O	CO_2	CO	Ar
vH2	59.22%	19.74%			21.05%
(vary H_2)	35.53%	19.74%			44.73%
	11.84%	19.74%			68.42%
vH2O	24.67%	59.22%			16.11%
(vary H_2O)	24.67%	24.67%			50.65%
	24.67%	9.87%			65.46%
vCO2	9.87%	4.93%	49.35%	19.74%	16.11%
(vary CO_2)	9.87%	4.93%	24.67%	19.74%	40.78%
	9.87%	4.93%	9.87%	19.74%	55.59%
vCO	9.87%	4.93%	19.74%	49.35%	16.11%
(vary CO)	9.87%	4.93%	19.74%	24.67%	40.78%
	9.87%	4.93%	19.74%	9.87%	55.59%

The thermal chemistry on the Ni and YSZ surfaces (Table 4, Table 5) are taken from previous work and therefore have well established rate data. Because of this, these parameters are not changed in the model to match experimental data. The charge-transfer mechanisms (Table 6, Table 7) are the primary means of matching the model to experimental data. There are three adjustable parameters in the rate expressions for the rate-limiting charge-transfer reactions that are modified to find best fit with measured polarization data. These parameters are the pre-exponential factor (A), the activation energy (E), and the anodic symmetry factor (β_a). The best

fit parameters for all operating conditions (i.e., all fuel compositions in Table 8 and all operating temperatures) are shown in Table 6 and Table 7.

5.1 H_2-H_2O Mixture Polarization Behavior

The most-basic fuel composition is that solely of steam and hydrogen. These are referred to as case vH_2 and vH_2O in Table 8. Figure 12 and Figure 13 show the polarization results for various H_2-H_2O compositions at the fixed temperature of 850 °C. The polarization data is shown in Tafel form as the log of current density as a function of operating voltage. The left-side branch, where V > OCV, shows electrolysis operation, where the cell consumes electric current. The right-side branch, V < OCV, indicates fuel-cell operation, where electric current is generated. The Tafel plot shows the absolute value of the current density, due to the logarithmic scale, but the actual current density for electrolyzer operation is negative, as the current direction is reversed from fuel-cell operation.

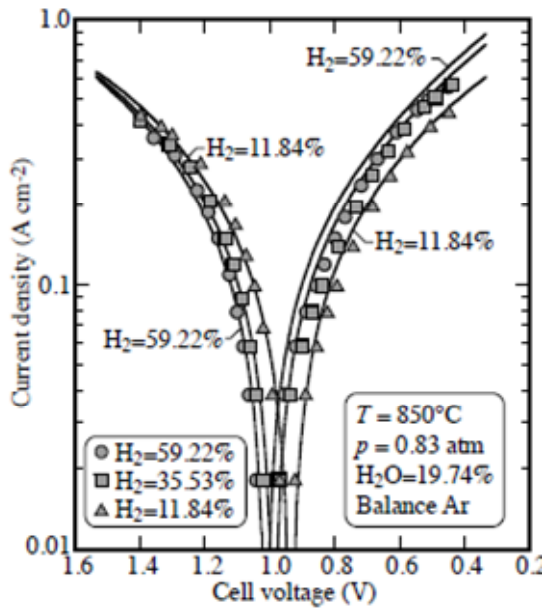

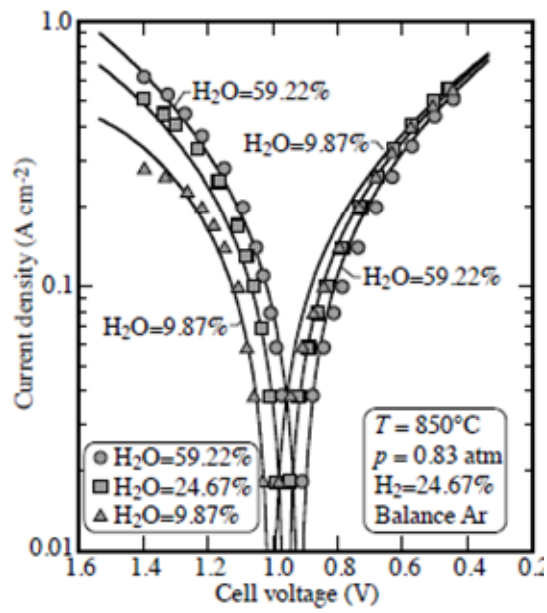

Figure 12 (Left): Comparison of polarization characteristics between model and experimental measurements for H2-H_2O mixtures. The partial pressure of H_2O is fixed, with the varying H_2 partial pressure balanced by Ar. The system is isothermal at 850 °C and 0.83 atm. The cha charge-transfer model considers only the hydrogen-spillover mechanism.

Figure 13 (Right): Comparison of polarization characteristics between model and experimental measurements for vH_2O case. The charge-transfer model considers only the hydrogen-spillover mechanism.

As expected, with an increase in H_2O content or decrease in H_2, the open circuit voltage decreases. The exact value of the OCV cannot be seen in the Tafel plot because of the logarithmic scale. However, the trend is easily visible. There is a smooth transition between operation in fuel-cell mode to electrolysis mode and no discontinuities are observed. The smooth transition between operational bias implies that the chemistry in the cell does not abruptly change between fuel-cell and electrolysis operation. This is seen in the Tafel plot as fairly

symmetric polarization on either side of OCV. At high polarization, however, the symmetry is not as evident, with one branch becoming steeper than the other.

Both Figure 12 and Figure 13 only use the hydrogen-spillover charge transfer mechanism for charge-transfer chemistry (Table 6). The hydrogen-spillover mechanism is able to fit the measurements well. This is consistent with the findings of Goodwin et al. in matching Mizusaki data [22]. Only the 850 °C data is shown here, but lower temperatures display similar trends and fits. A qualitative examination of the plots shows the relative dependence on the variable fuel gas on each branch. The converging polarization curves on the cathodic branch of Figure 12 show a weak H2 reaction order in electrolysis operation. The parallel curves of the anodic branch indicate a significant dependence of H_2 partial pressure. Similarly, the parallel and diverging branches of Figure 13 indicate the dependence of H_2O on cell operation. There is a strong H_2O reaction order on the cathodic branch and a weak reaction order on the anodic branch.

5.2 Effect of CO/CO_2 Addition

A perhaps more-important application of the physical and electrochemical model is to understand the influence of CO and CO_2 on fuel-cell and electrolysis chemistry. Figure 14 and Figure 15 show polarization data in which the partial pressures of CO and CO_2 are varied, respectively, while H_2 and H_2O are held constant (referred to as vCO and vCO_2 in Table 8). For both systems the temperature is held at 850 °C and at a pressure of 0.83 atm.

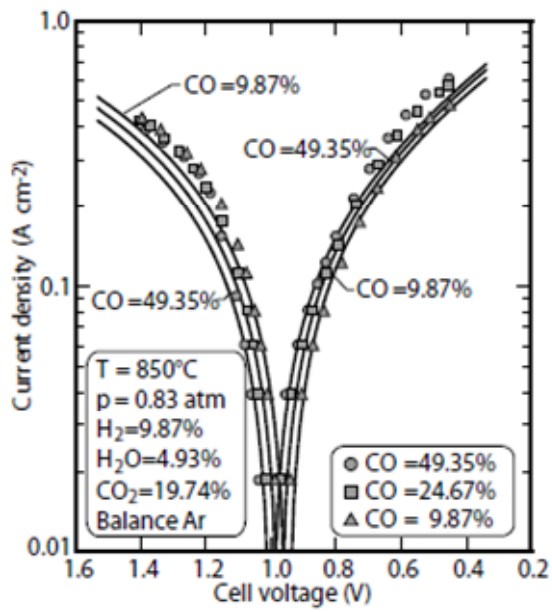

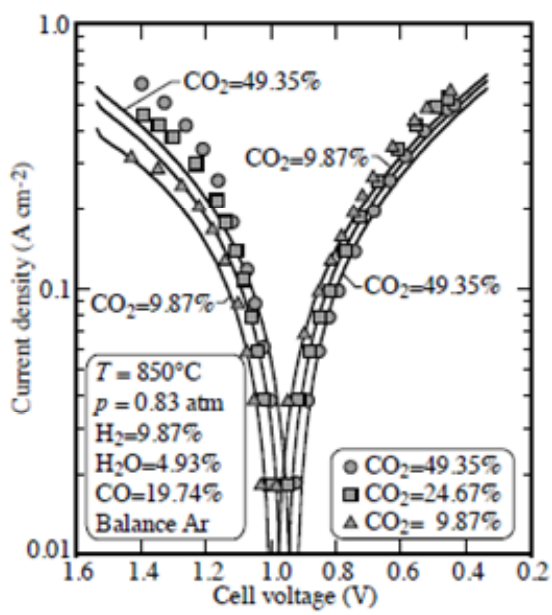

Figure 14 (Left): Comparison of polarization characteristics between model and experimental measurements for vCO case. The charge-transfer model considers only the hydrogen-spillover mechanism.

Figure 15 (Right): Comparison of polarization characteristics between model and experimental measurements for vCO2 case. The charge-transfer model considers only the hydrogen-spillover mechanism.

For results shown in Figure 14 and Figure 15, only the hydrogen-spillover charge transfer reaction mechanism is being used (Table 6). Using only this mechanism, all CO-CO_2 chemistry must proceed through thermal reactions. Water gas shift (WGS) reactions (globally, $CO + H_2O \leftrightarrow CO_2 + H_2$) proceed catalytically on the Ni surfaces and quickly convert CO and H_2O to CO_2 and H_2, and vice versa.

Figure 14 and Figure 15 reveal that the model tends to under-predict the measured current density, especially with cathodic polarization. In the case of variable CO fuel, the model predicts a significantly stronger dependence on the cathodic branch than shown experimentally. The converging data in Figure 14 indicates a low reaction order with respect to CO while operating as an electrolyzer.

5.3 Effect of Charge-Transfer Mechanism

The water-gas-shift chemistry is most likely not solely responsible for CO oxidation, as CO electro-oxidation is known to proceed without H_2. Therefore, it is likely that CO oxidation and CO_2 reduction in a high-temperature SOC utilizes an oxygen-spillover mechanism (shown in Table 7). It is possible that electro-oxidation and electro-reduction in a H_2-H_2O system employs an oxygen-spillover charge transfer mechanism, as well. However, this route is unlikely and hydrogen-spillover is probably dominant [22].

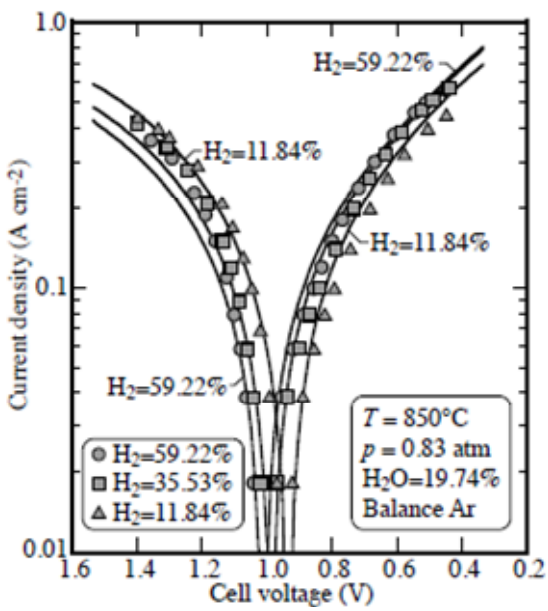

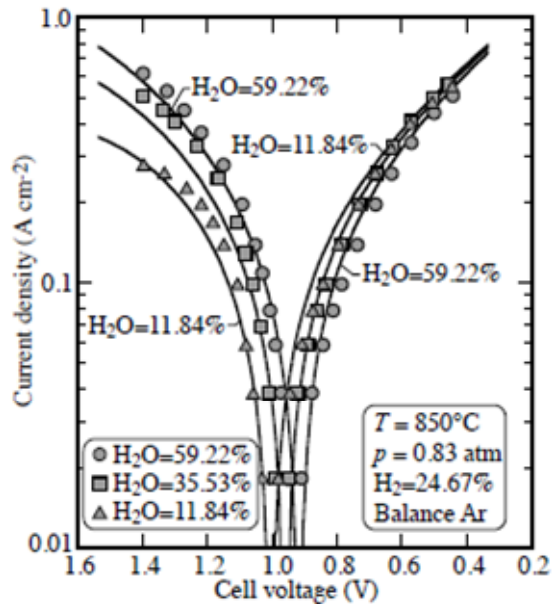

Figure 16 (Left): Comparison of polarization characteristics between model and experimental measurements for vH_2 case. The charge-transfer model considers only the oxygen-spillover mechanism.

Figure 17 (Right): Comparison of polarization characteristics between model and experimental measurements for vH2O case. The charge-transfer model considers only the oxygen-spillover mechanism.

The same experimental data for H_2-H_2O operation is shown in Figure 16 and Figure 17 as in Figure 12 and Figure 13, respectively. The latter two figures show the H_2-H_2O model represented only with the oxygen-spillover charge transfer mechanism, instead of the hydrogen-spillover.

The oxygen-spillover provides reasonable correlation between model and data, especially in the variable steam case (Figure 17). However, for variable H_2 partial pressure (Figure 16) the oxygen-spillover mechanism does not represent the H_2 reaction order well on the cathodic branch. Qualitatively, the hydrogen spillover (Figure 12) better matches the convergence of the polarization curves at high cathodic polarization.

The oxygen-spillover charge transfer mechanism is also applied to the co-electrolysis systems. Figure 18 and Figure 19 show the same measurements as Figure 14 and Figure 15, respectively, but use exclusively oxygen-spillover chemistry for charge-transfer. In both instances (vCO and vCO_2) the oxygen-spillover mechanism better represents the data as compared to the hydrogen-spillover mechanism shown in Figure 14 and Figure 15. The anodic branch produces a better fit. The cathodic branch, while better matched, still under-predicts the measured current density. With variable CO partial pressure, the cathodic branch is still predicted to have parallel polarization curves while the data converges.

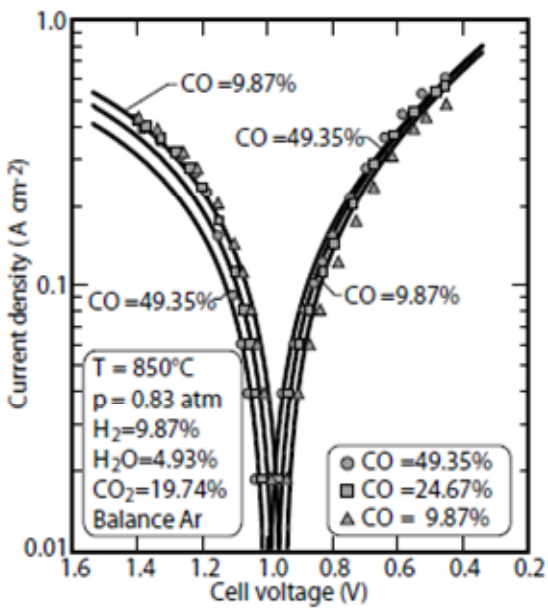

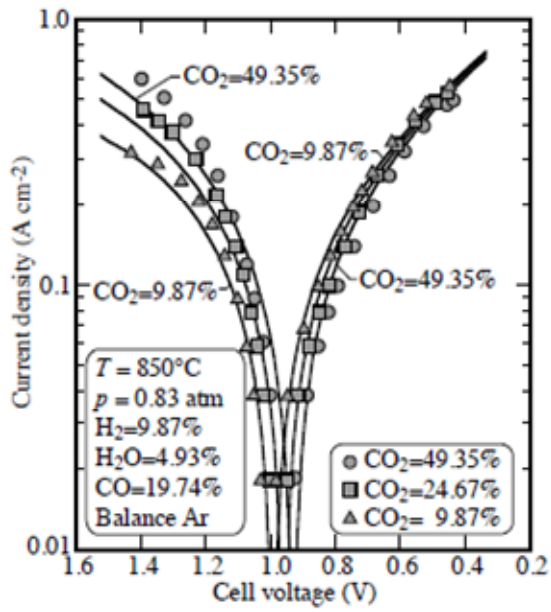

Figure 18 (Left): Comparison of polarization characteristics between model and experimental measurements for vCO case. The charge-transfer model considers only the oxygen-spillover mechanism.

Figure 19 (Right) : Comparison of polarization characteristics between model and experimental measurements for vCO_2 case. The charge-transfer model considers only the oxygen-spillover mechanism.

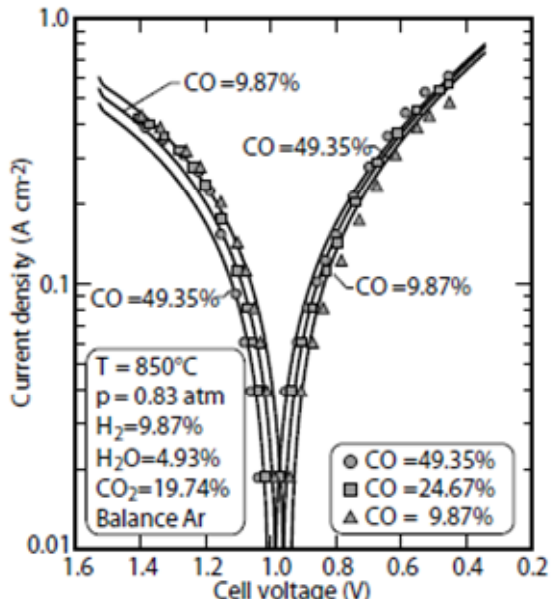

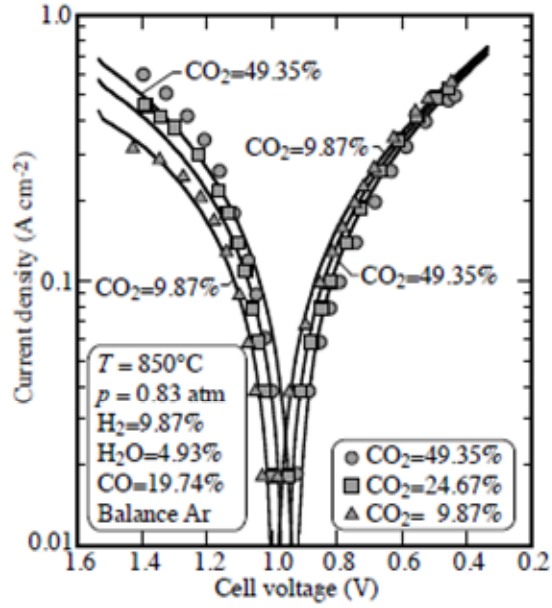

Figure 20 (Left): Comparison of polarization characteristics between model and experimental measurements for vCO case. The charge-transfer model considers both the hydrogen- and oxygen-spillover mechanism.

Figure 21 (Right): Comparison of polarization characteristics between model and experimental measurements for vCO_2 case. The charge-transfer model considers both the hydrogen- and oxygen-spillover mechanism.

Because there is a good possibility that multiple charge-transfer mechanisms are proceeding in parallel, a comparison is made to the data with both hydrogen-spillover and oxygen-spillover channels active. Figure 20 and Figure 21 show the same data as previous vCO and vCO_2 cases, but with both charge-transfer mechanisms (Table 6 and Table 7).

In both cases for co-electrolysis the dual charge-transfer mechanisms in parallel represent the data better than either mechanism alone. This supports the case that multiple pathways are available for charge-transfer at the triple-phase boundary. The final values for the adjustable model parameters are given in Table 6 and Table 7. These values yield the best fit for all cases shown in Table 8 and at all testing temperatures (750, 800, 850 °C).

5.4 Analysis of Rate-Limiting Charge-Transfer Reactions

The model now has a high correlation to the experimental data, so pure modeling results should be valid to analyze the effect of each charge-transfer mechanism on cell performance. This modeling work was performed by Dr. Huayang Zhu, but the results are very relevant to this paper. The importance of each charge-transfer pathway can be evaluated by calculating the contribution to electric current from each of the rate-limiting charge-transfer reaction steps. The current for each reaction is evaluated as

$$i_i = 2\pi \int_{R_{in}}^{R_{out}} \lambda_{TPB}^{V} i_{e,i} r dr. \tag{5.1}$$

The contribution of each mechanism is shown in Figure 22 for vCO_2 at the relative high and low temperatures of the experiment. It is seen that at high temperature, the oxygen-spillover pathway dominates the charge-transfer process with high CO_2 partial pressures. At low CO_2 partial pressures, both mechanisms are comparable in the cathodic branch, and there is little change in the anodic branch. At 750 °C, the relative importance is much different. Here, the hydrogen-spillover pathway is dominant with all levels of CO_2. As expected, all rates are lower at 750 °C than at 850 °C.

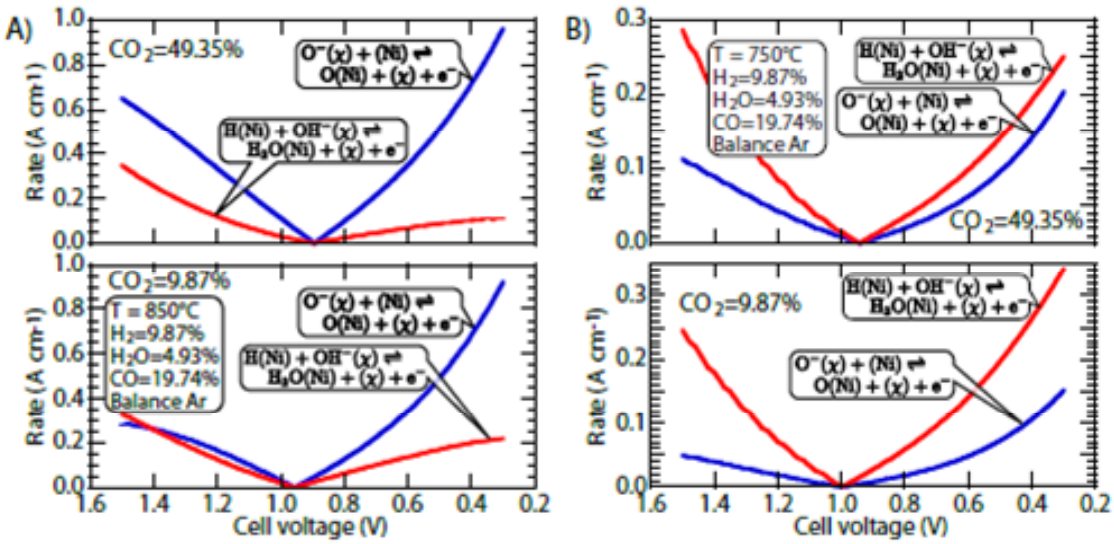

Figure 22: Comparison of the currents produced by each rate-limiting charge-transfer reaction step at A) 850 °C and B) 750 °C. The partial pressure of CO is fixed, and the varying CO_2 partial pressure is balance by Ar. The system is at 0.83 atm.

There seem to be significant differences in the dominant charge-transfer steps depending on the operating conditions. However, because the two pathways yield comparable results, it can be expected that the detailed pathways are sensitive to small variations in the charge-transfer rate parameters. While qualitative arguments can be given to explain the roles of each separate pathway, more direct measurements of each specific reaction are needed to be quantitatively definitive about the results.

5.5 Temperature Dependence

Charge-transfer rates depend heavily on the temperature at which the reactions occur. The amount of dependence depends on the operating conditions-- both the gas composition and the cell voltage. Activation energies in the model can be adjusted such that there is agreement in the model both at high and low temperatures. Figure 21 shows that the model for the vCO_2 case at 750 °C is quite close to the experimental data. This is also witnessed for the other gas compositions.

The global activation energies are found to be on the order of 100 kJ/mol. The Arrhenius plot in Figure 22 shows the temperature dependence for the fuel mixture of 9.87% H_2, 4.93% H_2O, 24.67% CO, and 19.74% CO_2 at various operating potentials. The polarization is clearly

activated, but does not vary greatly as a function of cell voltage. Less current is needed to deliver the requisite activation energy at higher temperatures, as the thermal energy contribution grows. The ohmic resistance through the YSZ electrolyte is activated at 80 kJ mol^{-1} and the air-electrode charge transfer is activated at 140 kJ mol^{-1}. These numbers are large compared to the 50 kJ mol^{-1} used for the fuel-electrode charge-transfer reactions (Table 6 and Table 7). Even though the 50 kJ mol^{-1} activation energy is found to deliver good modeling results for the measured polarization, the electrolyte ohmic resistance and the air-electrode charge-transfer dominate the overall temperature dependence.

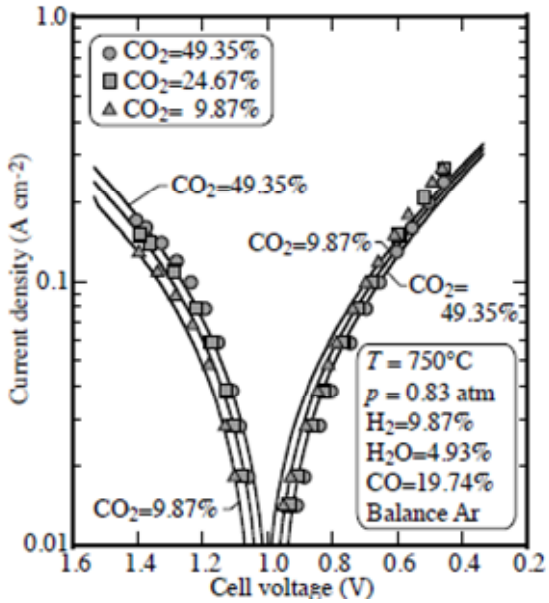

Figure 23: Comparison of polarization characteristics between model and experimental measurements for vCO2 case. The system is isothermal at 750 °C. The charge-transfer model considers both the hydrogen- and oxygen-spillover mechanism.

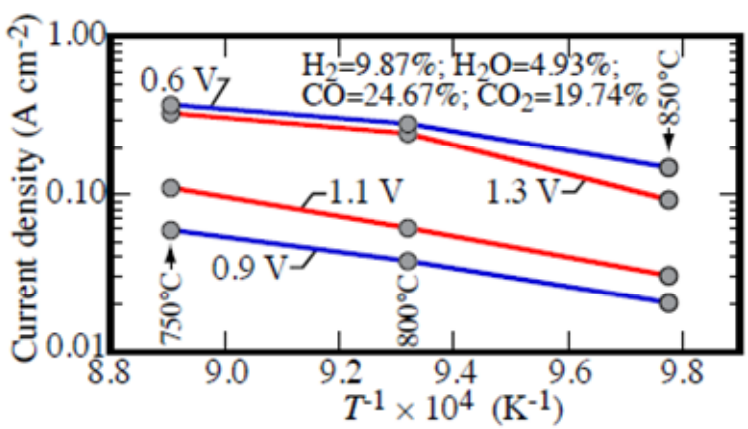

Figure 24: Current density as a function of temperature (Arrhenius form) for indicated operating condition.

6. CONCLUSIONS

In this report, the concept of and motivation for researching high temperature solid-oxide electrolysis cells were developed. Syngas production through high-temperature electrolysis was shown to be a viable option through exploration of other existing technologies. Previous research that forms the basis of understanding for this paper, including patterned anode experiments and modeling attempts, was explored.

The performance of a tubular solid-oxide cell was characterized using polarization measurements in operation as a fuel cell and as an electrolyzer. A cell fabricated with a Ni-YRSZ fuel-electrode support, YSZ electrolyte, and LSM-YSZ air-electrode was supplied a gas mixture of varying composition of H_2, H_2O, CO, CO_2, and Ar. Experiments used carefully controlled gas-phase partial pressures to assist in understanding reaction orders. The partial pressure of one gas species was varied, while all others were held fixed by balancing with Ar. High flow rates were used to assure low fuel utilization, thus matching the one-dimensional model with fixed fuel-channel mole fractions.

Experiments were interpreted via detailed reaction mechanisms. A model with fixed thermal chemistry and air-electrode charge-transfer chemistry and adjustable parameter charge-transfer mechanisms was used in matching experimental data. It was found that a parallel system of hydrogen- and oxygen-spillover charge-transfer provided the best fit for the data over all operating temperatures and gas compositions. By studying the individual contribution of the rate limiting reaction for each charge-transfer pathway separately, it was found that the oxygen-spillover mechanism is more important at high temperatures and high levels of CO_2. At low temperatures, the hydrogen-spillover mechanism is dominant. Further work must be done, however, to fully quantify the contribution of each separate mechanism and the sensitivity to various modeling parameters.

6.1 Improvements

Throughout the course of experimentation several tests were repeated, cells broken, and problems encountered. Although many of these problems were corrected, there are still improvements that can be made on the setup of the experiment.

Upon cooling and post-mortem analysis of the cells tested, most had carbon deposition on the anode closer to the exhaust side. While this in itself is not troubling, as species with carbon are present, further investigation shows that these deposits should not exist. Analysis using a one-dimensional anode model in CANTERA shows that under the fuel compositions tested, solid carbon formation is not thermodynamically predicted. There should not be any carbon deposited anywhere within the anode. However, likely the cause of this carbon build up was a cooler temperature region on the back half of the cell combined with an increase C/O ratio from exhaust gases during cell operation. This will have to be confirmed.

The gas compositions used were designed around minimizing utilization while maximizing the spread in the gas varied. Setting a high point for utilization requires that a certain flow rate of every gas must be supplied at all times, so as to not create additional losses. The utilization sets a

low point for gas supply, but the high point is limited only by mass-flow-controller capacity. In order to create a larger spread of data, higher capacity mass flow controllers could be used and the total flow rate could be increased while maintaining the same partial pressures.

6.2 Future Direction

The work explained in this paper provides a starting point in analyzing the charge-transfer process in high temperature solid-oxide electrolysis cells. Significant qualitative results were drawn from matching the experimental data to the model; however, future work in electrolysis cells can further understanding. Specific experiments may be designed to isolate the various charge transfer reactions and directly measure the effect of each quantitatively. Such direct measurements could confirm or disprove the qualitative conclusions drawn here.

To test the robustness of the model, planar cells could be used to confirm the results with different geometries. If the model developed herein only works with tubular cells of specific dimensions, it's application is limited. Application to different materials is difficult at the moment, as heterogeneous reactions mechanisms are not well established for emerging material choices. The Ni-YSZ cermet anode has well-established heterogeneous thermal chemistry and modeling has been applied to the material for the last decade or more. As reaction mechanisms are developed though, they can be applied within this model, utilizing the porous media transport and geometry already in place.

7. REFERENCES

[1] R. O'Hayre, S.W. Cha, W. Colella, and F.B. Prinz. *Fuel Cell Fundamentals*. Wiley, 2006.

[2] A.O. Isenberg. Energy conversion via solid oxide electrolyte electrochemical cells at high temperatures. *Solid State Ionics*, 3/4:431-437, 1981.

[3] J. Guan, N. Minh, B. Ramamurthi, J. Ruud, J.H. Hong, P. Riley, and D. Weng. High performance exible reversible solid oxide fuel cell. Technical report, GE Global Research Center, 2000.

[4] M. Ni, M.K.H. Leung, and D.Y.C. Leung. Technological development of hydrogen production by solid oxide electrolyzer cell (SOEC). *International Journal of Hydrogen Energy,* 33:2337-2354, 2008.

[5] S.H. Jensen, P.H. Larsen, and M. Mogensen. Hydrogen and synthetic fuel production from renewable energy sources. *International Journal of Hydrogen Energy*, 32:3253-3257, 2007.

[6] C. Stoots, J. O'Brien, and J. Hartvigsen. Results of recent high temperature coelectrolysis studies and the Idaho National Laboratory. *International Journal of Hydrogen Energy*, 34:4208-4215, 2009.

[7] C. Stoots, J.E. O'Brien, K.G. Condie, and J.J. Hartvigsen. High-temperature electrolysis for large-scale hydrogen production from nuclear energy- Experimental investigations. *International Journal of Hydrogen Energy*, 35: 4861{4870, 2010.

[8] X. Yang and J.T.S. Irvine. $(La_{0:75}Sr_{0:25})_{0:95}Mn_{0:5}Cr_{0:5}O_3$ as a cathode of solid oxide electolysis cells for high temperature hydrogen production from steam. *Journal of Materials Chemistry*, 18:2349-2354, 2008.

[9] W. Wang, Y. Huang, S. Jung, J.M. Vohs, and R.J. Gorte. A comparison of LSM, LSF, and LSCo for solid oxide electrolyzer anodes. *International Journal of Hydrogen Energy*, 153(11):A2066-A2070, 2006.

[10] J. Mizusaki, H. Tagawa, and T. Saito. Preparation of nickel pattern electrodes on YSZ and their electrochemical properties in H2-H2O atmospheres. *Journal of the Electrochemical Society*, 141(8):2129-2134, 1994.

[11] J. Mizusaki, H. Tagawa, T. Saito, and T. Yamamura. Kinetic studies of the reaction at the nickel pattern electrode on YSZ in H_2-H_2O atmospheres. *Solid State Ionics*, 70/71:52-58, 1994.

[12] A.M. Sukeshini, B. Habibzadeh, B.P. Becker, C.A. Stoltz, B.W. Eichhorn, and G.S. Jackson. Electrochemical oxidation of H_2, CO, and CO/H_2 mixtures on patterned Ni anodes on YSZ electrolytes. *Journal of the Electrochemical Society*, 153(4):A705-A715, 2006.

[13] M. Steinberg and H.C. Cheng. Modern and prospective technologies for hydrogen production from fossil fuels. *International Journal of Hydrogen Energy*, 14(11):797-820, 1989.

[14] Y. Shin, W. Park, J. Chang, and J. Park. Evaluation of the high temperature electrolysis of steam to produce hydrogen. *International Journal of Hydrogen Energy*, 32:1486-1491, 2007.

[15] R. Hino, K. Haga, H. Aita, and K. Sekita. R&D on hydrogen production by high-temperature electrolysis of steam. *Nuclear Engineering and Design*, 233: 363{375, 2004.

[16] V. Utgikar and T. Thiesen. Life cycle assessment of high temperature electrolysis for hydrogen production via nuclear energy. *International Journal of Hydrogen Energy*, 31:939-944, 2006.

[17] K. Huang and J.B. Goodenough. A solid oxide fuel cell based on Sr- and Mg- doped LaGaO3 electrolyte: the role of a rare-earth oxide buffer. *Journal of Alloys and Compounds*, 303-304:454-464, 2000.

[18] D. Storjohann, J. Daggett, N.P. Sullivan, H. Zhu, R.J. Kee, S. Menzer, and D. Beea_. Fabrication and evaluation of solid-oxide fuel cell anodes employing reaction-sintered yttria-stabilized zirconia. *Journal of Power Sources*, 193: 706-712, 2009.

[19] A. Hauch, S.H. Jensen, S.D. Ebbesen, and M. Mogensen. Durability of solid oxide electrolysis cells for hydrogen production. Technical report, Risoe National Laboratory, Technical University of Denmark.

[20] A. Hauch, S.H. Jensen, S. Ramousse, and M. Mogensen. Performance and durability of solid oxide electrolysis cells. *Journal of the Electrochemical Society*, 153(9):A1741-A1747, 2006.

[21] A. Hauch, S.D. Ebbesen, S.H. Jensen, and M. Mogensen. Solid oxide electrolysis cells: Microstructure and degradation of the Ni / yttria-stabilized zirconia electrode. *Journal of the Electrochemical Society*, 155(11): B1184-B1193, 2008.

[22] D.G. Goodwin, H. Zhu, A.M. Colclasure, and R.J. Kee. Modeling electrochemical oxidation of hydrogen on Ni-YSZ pattern anodes. *Journal of the Electrochemical Society*, 156(9):B1004-B1021, 2009.

[23] R. Swartzlander and W.G. Coors. Preparation of yttria-stabilized zirconia reaction sintered products. United States Patent 20070176332, 2007.

[24] E. Mason and A. Malinauskas. *Gas Transport in Porous Media: the Dusty-Gas Model*. American Elsevier, New York, 1983.

[25] H. Zhu, R.J. Kee, V.M. Janardhanan, O. Deutschmann, and D.G. Goodwin. Modeling elementary heterogeneous chemistry and electrochemistry in solid-oxide fuel cells. *Journal of the Electrochemical Society,* 152(12): A2427-A2440, 2005.

[26] H. Zhu and R.J. Kee. Modeling distributed charge-transfer processes in SOFC membrane electrode assemblies. *Journal of the Electrochemical Society*, 155(7): B715-A729, 2008.

[27] D. Chen, Z. Lin, H. Zhu, and R.J. Kee. Percolation theory to predict effective properties of solid oxide fuel-cell composite electrodes. *Journal of Power Sources*, 191:240-252, 2009.

[28] E.S. Hecht, G.K. Gupta, H. Zhu, A.M. Dean, R.J. Kee, L. Maier, and O. Deutschmann. Methane reforming kinetics within a Ni-YSZ SOFC anode support. *Applied Catalysis A, 295(1):40-51, 2005.*

[29] V.M. Janardhanan and O. Deutschmann. CFD analysis of a solid oxide fuel cell with internal reforming: coupled interactions of transport, heterogeneous catalysis and electrochemical processes. *Journal of Power Sources*, 162: 1192-1202, 2006.

DISTRIBUTION

1	MS0734	Ellen Stechel	6364 (electronic copy)
1	MS0734	Andrea Ambrosini	6364 (electronic copy)
1	MS0899	Technical Library	9536 (electronic copy)

For LDRD reports, add:

1	MS0123	D. Chavez, LDRD Office	1011 (electronic copy)

Sandia National Laboratories